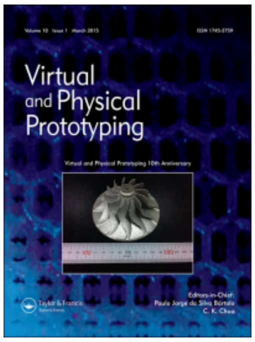

Virtual and Physical Prototyping

ISSN: (Print) (Online) Journal homepage: www.tandfonline.com/journals/nvpp20

Oscillatory nature in melt-gas-powder interactions during laser powder bed fusion process revealed by CFD-DEM coupled modelling

Weihao Yuan, Hui Chen, Siyuan Ruan, Rocco Lupoi, Shaocong Qin, Enyu Guo, Jianfeng Wang & Shuo Yin

To cite this article: Weihao Yuan, Hui Chen, Siyuan Ruan, Rocco Lupoi, Shaocong Qin, Enyu Guo, Jianfeng Wang & Shuo Yin (2025) Oscillatory nature in melt-gas-powder interactions during laser powder bed fusion process revealed by CFD-DEM coupled modelling, Virtual and Physical Prototyping, 20:1, e2446619, DOI: 10.1080/17452759.2024.2446619

To link to this article: https://doi.org/10.1080/17452759.2024.2446619

Published online: 15 Jan 2025.

VIRTUAL AND PHYSICAL PROTOTYPING
2025, VOL. 20, NO. 1, e2446619 (24 pages)
https://doi.org/10.1080/17452759.2024.2446619

Oscillatory nature in melt-gas-powder interactions during laser powder bed fusion process revealed by CFD-DEM coupled modelling

Weihao Yuan[a], Hui Chen[b], Siyuan Ruan[a], Rocco Lupoi[a], Shaocong Qin[a], Enyu Guo[c], Jianfeng Wang[a,d] and Shuo Yin[a]

[a]Department of Mechanical, Manufacturing and Biomedical Engineering, Trinity College Dublin, The University of Dublin, Dublin 2, Ireland; [b]State Key Laboratory of Solidification Processing, Northwestern Polytechnical University, Xi'an, People's Republic of China; [c]Key Laboratory of Solidification Control and Digital Preparation Technology, School of Materials Science and Engineering, Dalian University of Technology, Dalian, People's Republic of China; [d]College of Materials Science and Technology, Nanjing University of Aeronautics and Astronautics, Nanjing, People's Republic of China

ABSTRACT
The laser powder bed fusion (LPBF) process encompasses interactions between different material states, including melt, gas, and powder. While observational techniques can capture specific states, they cannot be combined to produce a comprehensive monitoring how they are mutually interacted. Thus, an integrated modelling approach is a crucial solution for revealing their interactions. This study investigates melt-gas-powder dynamics under varying laser scan speeds through a coupled CFD-DEM multiphase model. Findings reveal that metal vapour consistently transitions from an initialisation phase to a processing phase, exhibiting consistent behaviour in the former but varied responses in the latter. A relationship is identified between scan speed and vapour flow angle (VFA), with higher speeds broadening the VFA. Significantly, three oscillatory behaviours are observed: first, the oscillation of locally intensified pressure (LIP) sites on keyhole walls, where vapour ejection modes shift and may become periodic at intermediate scan speeds; second, the oscillation of two induced argon vortex flows with opposite swirling directions; and third, a simultaneously induced varying drag force on powder spatter. These oscillations clarify various spatter mechanisms, offer insights for process optimisation, and suggest implications for process stability. The study also proposes future research directions to further elucidate these mechanisms.

ARTICLE HISTORY
Received 4 November 2024
Accepted 19 December 2024

KEYWORDS
Coupled CFD-DEM model; vapour phase; locally intensified pressure; vortex flow; drage force

1. Introduction

As one of the foremost additive manufacturing (AM) technologies [1], laser powder bed fusion (LPBF) process can fabricate metal parts with extremely complex structure subject to human's imagination; this empowers LPBF enormous potential to be applied in a variety of sectors [2]. However, a major obstacle to the widespread application of LPBF stems from the sophisticated and uncontrollable physical phenomena. During the LPBF process, three material states are involved: liquid (melt), gas (metal vapour and shielding gas) and solid (powder), all of which are interconnected. Exploring the underlying interaction mechanisms can enhance understandings of LPBF and offer valuable insights for process optimisation.

wTo date, no experimental apparatus has been capable of capturing all the aforementioned material states simultaneously, nor fully identifying the melt-gas-powder interaction during LPBF process. Alternatively, researchers focus on individual or partial states through in-situ or ex-situ observational techniques. One method is using X-ray synchrotron imaging [3-10], by which Guo et al. [3] identified powder spattering phenomenon, and they quantified vapour-driven and argon-driven powder dynamics. Qiu et al. [4] focused on the effects of spatter defects, and correlated it with the process stability. They proposed using nanoparticles which can create capillary pressure barrier to increase the melt pool stability and prevent the formation of large liquid agglomerated spatter. With similar experimental instruments, the porosity dynamics also receives substantial interests, which is often related to the formation of a keyhole [5]. Hojjatzadeh et al. [6] reported that thermal capillary force induced by thermal gradient may help eliminate pores.

CONTACT Shuo Yin yins@tcd.ie Department of Mechanical, Manufacturing and Biomedical Engineering, Parsons Building, Trinity College Dublin, The University of Dublin, Dublin 2, Ireland

To quantify the keyhole stability, Gan et al. [7] established scaled laws by linking the melt pool aspect ratio with their defined keyhole number, the latter involves processing parameters and material properties. Similarly, Huang et al. [8] investigated the relationship between the evolutions of keyhole and induced pores, and it is observed that pores form predominantly at the rear keyhole wall. Also, Zhao et al. [10] reported a new formation mechanism and driving force for the keyhole induced pores. Their study also demonstrated that few variations can be observed whether laser impacts on powder bed or bare plate. From a more general perspective, Cunningham et al. [9] defined the threshold for the transitions from conduction mode to keyhole model. However, one limitation of using synchrotron X-ray imaging is the inability to identify metal vapour. Additionally, the observation region is restricted to two dimensions due to the transmission properties of X-rays. The absence of an isometric view may reduce the credibility of the results to some extent [11]. A case in point is the denudation phenomenon [12,13], which can only be clearly inspected from a top view.

Consequently, some studies were conducted shifting the focus on top or isometric views of the LPBF process. The research conducted by Matthews et al. [13] is the pioneer for identifying denudation defect via an in-situ characterisation experiment. Bidare et al. [14] further identified three different patterns of denudation dependent of different processing parameters. They also proposed employing schlieren imaging technique to characterise the laser plume/vapour [15]. With similar instruments, Yin et al. [16], reported that the backward liquid ejection is attributed to vapour impacting on the melt pool and the backward powder spatter is driven by metal vapour. Further, Bitharas et al. [17] combined in-situ synchrotron X-ray with schlieren imaging to investigate the interplay between metal vapour, liquid melt and powder. They raised that the plume morphology can be used as an indicator to evaluate the keyhole stability. Another approach to identify the powder spatter and metal vapour is utilising a high-speed camera. Instead of explicitly identifying the metal powder or vapour, attentions are paid on the outlines of laser plume and spatter, which derive from the reflected light induced by laser-material interaction. For example, Zheng et al. [18] captured laser plume and reported that the plume behaviour is majorly dominated by laser scan speed. They also observed that powder particles incur the main source of spatter. A similar in-situ monitoring apparatus was adopted in a recent research by Wang et al. [19]. They correlated the different melting mode with the evolutions of plume and spatter. Zhang et al. [20] developed a machine learning model to establish the relationship between processing parameters and optical reflections including the features of laser plume, spatter and melt pool, to facilitate online quality monitoring. Liu et al. [21] extracted the features of droplet spatter by an image processing method and correlated it with shielding gas flow parameters.

Unfortunately, it is virtually impossible to experimentally identify the dynamic behaviours of the three aforementioned material states, namely, the melt pool, gas, and powder spatter, in a simultaneous manner. Therefore, it is advisable to develop an advanced high-fidelity physics-based model to realise observation. A common approach is to employ computational fluid dynamics (CFD) to study melt pool dynamics [22-33] and use discrete element method (DEM) to investigate powder behaviours [34-36]. However, nearly all related studies treat these two systems separately. As one of the consequences, although the evaporation of the melt pool is considered, the resulting vapour does not influence powder behaviours [37-39]. Many research have highlighted the challenge of modelling the complex interactions among the melt pool, gas flow and powder spatter [19,40]. To the best of our knowledge, only a few studies have developed coupled models to address these interconnected phenomena. Chen et al. [41,42] were the first to build up a model involving both powder spatter and metal vapour. Similar research was conducted by Trong et al. [43], who improved Chen's model by incorporating the 'powder absorption' effects. However, these studies relied on artificially simulating vapour ejection based on an empirical values rather than explicitly modelling metal vapour through the CFD method. The model developed by Li et al. [44,45] is able to identify the simultaneous evolution of the melt pool, metal vapour, and powder under a stationary laser. However, real LPBF processing conditions, such as laser scan speed and laser power, were not incorporated. Yu et al. [46] developed a CFD-DEM coupled model with a moving laser. However, no correlations were disclosed among melt-gas-powder interactions, as the attentions remained primarily on melt pool behaviours. Also, the effects of processing parameters on the melt-gas-powder interactions were not explored. Another concern is that both Li and Yu employed the immersed boundary/fictitious domain [47] to resolve the powder-liquid conversion. This may increase the difficulty of model generalisation as their studies do not offer a comprehensive view of the melt-gas-powder interactions, although being more complicated in terms of modelling procedure. Therefore, it would be valuable that an coupled model can be developed, capable of identifying the melt-gas-powder interactions while considering a wide range of LPBF process conditions. As will be demonstrated, many of the phenomena that are to be produced are documented for the first time and can establish explanatory connections with existing literatures.

The rest of this paper is structured as follows: Section 2 details the modelling framework. Section 3 displays simulation results at different laser scan speeds, focusing on vapour and powder behaviours, assisted by experimental observations. Section 4 investigates three dynamic relationships within the melt-gas-powder system, linking the observed oscillatory nature to process stability and suggesting future research directions. Section 5 concludes the study.

2. Modelling

2.1. CFD system

It is emphasised here that it is the positive net element flux (j^{net}) from the gas–liquid interface that induces the 'recoil pressure' effect [48], and is described by Hertz-Knudsen formula [49] as:

$$j^{net} = \phi \cdot p_s \sqrt{\frac{m_A}{2\pi \cdot k_B T}} \tag{1}$$

where m_A, k_B and T represent atomic mass, Boltzmann constant and surface temperature, respectively. ϕ represents evaporation coefficient [50], and p_s is the saturated vapour pressure. The latter can be derived from Clausius–Clapeyron equation, which correlates saturated pressure with surface Based on constant evaporation latent heat, the saturated pressure is expressed as:

$$p_s = \mathrm{p_0} \exp\left[\frac{\mathrm{L_v} m_A}{k_B}\left(\frac{1}{\mathrm{T_v}} - \frac{1}{T}\right)\right] \tag{2}$$

where $\mathrm{p_0}$, $\mathrm{L_v}$ and $\mathrm{T_v}$ represent atmospheric pressure, evaporation latent heat and boiling point. In this way, the mass transfer rate due to the melt evaporation can be expressed as [7]:

$$m_{LG} = \phi \cdot \mathrm{p_0} \exp\left[\frac{\mathrm{L_v M_{F1}}}{\mathrm{R_u}}\left(\frac{1}{\mathrm{T_v}} - \frac{1}{T}\right)\right]\sqrt{\frac{\mathrm{M_{F1}}}{2\pi \mathrm{R_u} T}}|\nabla \alpha_{\mathrm{F1}}|\frac{2\rho_{\mathrm{F}}}{\rho_{\mathrm{F1}} + \rho_{\mathrm{F2}}} \tag{3}$$

where ρ_{F}, ρ_{F1}, and ρ_{F2} represent averaged fluid density, liquid density and gas density. $\mathrm{M_{F1}}$ and $\mathrm{R_u}$ denote metal molar mass and universal gas constant.

To use Hertz-Knudsen formula, the gas should follow ideal gas state equation. Also note that the commonly used expression for 'recoil pressure' [51] should be deprecated, as will be seen in Eq. (7). By integrating the mass transfer rate with the VOF model [52], the continuity equation can be obtained:

$$\begin{cases} \dfrac{\partial \alpha_{\mathrm{F1}}}{\partial t} + \nabla \cdot (\alpha_{\mathrm{F1}} \boldsymbol{u}_{\mathbf{F}}) = \dfrac{-m_{LG}}{\rho_{\mathrm{F1}}} \\ \dfrac{\partial \alpha_{\mathrm{F2}}}{\partial t} + \nabla \cdot (\alpha_{\mathrm{F2}} \boldsymbol{u}_{\mathbf{F}}) = \dfrac{m_{LG}}{\rho_{\mathrm{F2}}} \\ \rho_{\mathrm{F2}} = \dfrac{p}{\mathrm{R_s} T} = \dfrac{p\mathrm{M_{F2}}}{\mathrm{R_u} T} \end{cases} \tag{4}$$

where $\boldsymbol{u}_{\mathbf{F}}$, α_{F1}, and α_{F2} represent fluid velocity, volume fraction of liquid and gas; $\mathrm{M_{F2}}$, p, and $\mathrm{R_s}$ represent gas molar mass, transient pressure, and universal gas constant, respectively.

To account for the evolution of the produced metal vapour as well as shielding gas, gas phase is modelled composed of argon and vapour constituent, represented by mass fraction β_i $(i = 1,\ 2)$ [14,41]. Thus, the thermophysical properties of gas, including viscosity, molar mass, specific heat and thermal conductivity are averaged by mass fraction. The governing equation for gas component concentration is expressed by Eq. (5), where $\mathrm{D_{F2}}$ denotes gas diffusivity [7]. In the mixture gas phase, vapour phase is defined here subject to its mass fraction over 0.5.

$$\frac{\partial}{\partial t}(\rho_{\mathrm{F2}} \alpha_{\mathrm{F2}} \beta_i) + \nabla \cdot (\boldsymbol{u}_{\mathbf{F}} \rho_{\mathrm{F2}} \alpha_{\mathrm{F2}} \beta_i) = \nabla \cdot (\rho_{\mathrm{F2}} \alpha_{\mathrm{F2}} \mathrm{D_{F2}} \nabla \beta_i) + m_{LG} \tag{5}$$

The traditional VOF model where liquid and gas share the velocity at the interface may not apply to where the vapour velocity can reach 100 times that of the liquid. Thus, Knudsen layer is proposed and can be approximated by slip velocity boundary, expressed as [45]:

$$V_{lt} - V_{gt} = \frac{\partial V_{lt}}{\partial \mathbf{n}} \cdot \frac{\mu_{\mathrm{F2}}}{\rho_{\mathrm{F2}}} \sqrt{\frac{\pi}{2\mathrm{R_s} T}} \tag{6}$$

where the left side of the equation is the slip velocity. V_{lt} and V_{gt} are the tangential velocity on the liquid and gaseous side of the interface. $\partial V_{lt}/\partial n$ represents the derivative of the gas tangential velocity with respect to the normal direction of the liquid–gas interface. The second term denotes the mean free path, where μ_{F2} and $\mathrm{R_s}$ denote the gas dynamic viscosity and specific gas constant, respectively.

The governing equations for momentum and energy conservations are expressed as:

$$\begin{cases} \frac{\partial}{\partial t}(\rho_F \boldsymbol{u}_F) + \nabla\cdot(\rho_F \boldsymbol{u}_F \otimes \boldsymbol{u}_F) \\ = -\nabla p + \nabla\cdot\left[\mu_F(\nabla \boldsymbol{u}_F + \nabla \boldsymbol{u}_F^T) - \frac{2}{3}\mu_F(\nabla\cdot \boldsymbol{u}_F)\mathbf{I}\right] + \boldsymbol{f}_{F-P} + \boldsymbol{S}_F \\ \frac{\partial}{\partial t}(\rho_F H) + \nabla\cdot(\boldsymbol{u}_F \rho_F H) = \nabla\cdot(k_F \nabla T) + q_{F-P} + q_{laser} - q_{loss} \end{cases} \tag{7}$$

where $\boldsymbol{f}_{F-P}$ and q_{F-P} denote the amount of momentum and heat, which are transferred from particle to fluid, and will be clarified later in Eq. (14). H, k_F and $\mathbf{I}$ are the specific enthalpy, fluid thermal conductivity and unit matrix; q_{laser} and q_{loss} represent laser heat and heat loss; these are expressed in Eq. (8). $\boldsymbol{S}_F$ denote other source terms induced by fluid and will be illustrated via Eq. (9);

$$\begin{cases} H = \int_{T_{ref}}^{T} c_F dT + (1-f_s)L_m \\ q_{laser} = \frac{2A_{ap}P}{\pi\omega^2}\exp\left(\frac{-r^2}{\omega^2}\right)|\nabla\alpha_{F1}|\frac{2\rho_F c_F}{\rho_{F1}c_{F1} + \rho_{F2}c_{F2}} \\ A_{ap} = 1 - \frac{1}{2}\left[\frac{1+(1-\varepsilon\cos\theta)^2}{1+(1+\varepsilon\cos\theta)^2} + \frac{\varepsilon^2 - 2\varepsilon\cos\theta + 2\cos^2\theta}{\varepsilon^2 + 2\varepsilon\cos\theta + 2\cos^2\theta}\right] \\ q_{loss} = q_c + q_r + q_{evp} = h_c(T - T_{ref}) + \sigma_s\varepsilon_r(T^4 - T_{ref}^4) + m_{LG}L_v \end{cases} \tag{8}$$

where T_{ref}, c_F and L_m denote reference temperature (300 K), fluid specific heat and latent heat of melting; A_{ap} denotes the transient laser absorptivity, which is correlated with laser incident angle θ and a material-specific coefficient related to electrical conductance, ε [53-55]. The solid volume fraction within the liquid–solid mixture is defined as $f_s = (T_L - T)/(T_L - T_S)$, where T_L and T_S are liquidus and solidus temperature. h_c denotes heat convection coefficient. The initial temperature for the CFD system is set to 300 K, with all other variables initialised to zero. The top boundary is defined as a pressure outlet at 1 atm, while the remaining boundary conditions for the computational domain are set to a constant temperature of 300 K.

The term $\boldsymbol{S}_F$ in the Eq. (7) is expressed as [28]:

$$\begin{cases} \boldsymbol{S}_F = \rho_F \mathbf{g} + \boldsymbol{f}_{st} + \boldsymbol{f}_{Marangoni} + \boldsymbol{f}_{Mushy} \\ \boldsymbol{f}_{st} = \sigma_{st}\cdot\nabla\mathbf{n}\cdot\mathbf{n} \\ \boldsymbol{f}_{Marangoni} = \frac{d\sigma_{st}}{dT}[\nabla T - \mathbf{n}(\mathbf{n}\cdot\nabla T)]|\nabla\alpha_{F1}|\frac{2\rho_F}{\rho_{F1}+\rho_{F2}} \\ \boldsymbol{f}_{Mushy} = \mu_F\left[\frac{A_{mush}f_s^2}{(1-f_s)^3 + C_1}\right]\boldsymbol{u}_F \end{cases} \tag{9}$$

where $\boldsymbol{f}_{st}$ and $\boldsymbol{f}_{Marangoni}$ represent surface tension and Marangoni force; σ_{st}, $\mathbf{n}$ and A_{mush} are surface tension coefficient, gas–liquid interface normal vector and Mushy zone number. Carman-Kozeny model [56] is used for the flow resistance ($\boldsymbol{f}_{Mushy}$) induced by the Mushy Zone. Note that A_{mush} used here is a converted version of shaper factor with unit [m^{-2}] based on Carman-Kozeny model, and C_1 is a small number to prevent division by zero. Besides, the liquid flow is suppressed on the condition of $f_s > 0.27$, which is based on the modified Metzner model [57].

2.2. DEM system

Each particle in terms of translation, rotation and energy are tracked in the computational domain via discrete element method (DEM). The governing equations are expressed as:

$$\begin{cases} m_p \frac{d\boldsymbol{u}_p}{dt} = \sum_{\epsilon} \mathbf{F}_d + (\mathbf{F}_g + \mathbf{F}_c) \\ \mathbf{I}_P \frac{d^2\boldsymbol{\theta}_P}{dt^2} = \sum_{\epsilon}(\mathbf{r}_c \times \mathbf{F}_c) \end{cases} \tag{10}$$

where $\boldsymbol{u}_p$, $\mathbf{F}_d$,. $\mathbf{F}_g$, and $\mathbf{F}_c$ denote particle velocity, drag force, gravity, and contact force; $\mathbf{I}_P$, $\boldsymbol{\theta}_P$, and $\mathbf{r}_c$ denote particle rotational inertia, angular displacement and position vector (from the particle centre of gravity to the particle contact point). The contact of two particles is modelled based on the Hertz-Mindlin theory [58]:

$$\begin{cases} \mathbf{F}_c = \sum_{\epsilon}(\mathbf{F}_n + \mathbf{F}_t) \\ \mathbf{F}_n = K_n\mathbf{d}_n + N_n\mathbf{v}_n \\ \mathbf{F}_t = \min(K_t\mathbf{d}_t + N_t\mathbf{v}_t\ ,\ C_{fs}\ |\mathbf{F}_n|) \\ K_n = \frac{2}{3}\cdot\left(\frac{E}{1-\sigma^2}\right)\cdot\sqrt{\frac{\mathbf{d}_n R_A R_B}{R_A + R_B}} \\ N_i = \left[\frac{5m_A m_B}{m_A + m_B}\cdot\frac{K_i}{1+\pi^2/\ln^2 C_r}\right]^{\frac{1}{2}} (i = n,\ t) \\ K_t = \frac{2E}{(2-\sigma)(1+\sigma)}\sqrt{\frac{\mathbf{d}_n R_A R_B}{R_A + R_B}} \end{cases} \tag{11}$$

where the drag force comprises normal and tangential components, denoted by $\mathbf{F}_n$ and $\mathbf{F}_t$, respectively; K_n, N_n, K_t, and N_t are particle normal stiffness, normal damping, tangential stiffness and tangential damping, respectively; $\mathbf{d}_n$ and $\mathbf{d}_t$ are normal and tangential displacement; $\mathbf{v}_n$ and $\mathbf{v}_t$ are normal and tangential velocity; E, σ, C_{fs} and C_r are used for particle Young's' modulus, Poisson ratio, static friction coefficient, and restitution coefficient, respectively.

It is highlighted that since the mass transfer from powder to liquid is not considered. In this way, the damping effect brought by $\boldsymbol{f}_{Mushy}$ in Eq. (9) does not influence powder behaviour. Besides, laser heat source is applied on powder particles, which is combined with linear heat conduction from particle-particle [59] and particle-fluid to account for energy conservation. The energy equation can be expressed as [60]:

$$\begin{cases} m_P c_P \dfrac{dT_P}{dt} = Q_{P-L} + \sum_{\epsilon} Q_{P-P} + \sum_{\epsilon} V_P q_{P-F} \\ Q_{P-P} = 2k_P \left(\dfrac{3\mathbf{F}_n r^*}{4E}\right)^{1/3} (T_A - T_B) \\ Q_{P-L} = \sum_{\epsilon} f(r_P^i, D_i) = \sum_{\epsilon} \dfrac{2C_2 P}{\pi D_i^2} \exp\left(\dfrac{-r_P^{i\,2}}{\omega^2}\right) \end{cases} \quad (12)$$

where Q_{P-L}, Q_{P-P}, V_P and q_{P-F} represent laser-induced heat, powder heat conduction, particle volume and fluid-induced heat rate, respectively; k_P and r^* represent particle thermal conductivity and geometric mean; r_P^i is the distance between the i^{th} particle centre of gravity and laser spot centre. ϵ denotes the particle domain; D_i is the i^{th} particle diameter. $C_2 = 0.4$ is an approximated laser absorptivity.

2.3. CFD-DEM coupling

Since particle phase is added to the Eulerian system, the realistic volume fraction for the fluid phase, α_{F_P}, is defined as the ratio of volume which is occupied by fluid phase to the specific cell volume. Thus, the particle volume fraction is $1 - \alpha_{F\_P}$ [61]. This study employs two-way coupling between fluid and particle phase, which implies that the transfer of momentum and heat are bi-directional between the two phases.

(1) From fluid to particle phase:

$$\begin{cases} \mathbf{F}_d = \dfrac{1}{2} C_d \rho_F \pi R_P^2 |\boldsymbol{u}_F - \boldsymbol{u}_P| (\boldsymbol{u}_F - \boldsymbol{u}_P) \\ q_{P-F} = h_{P-F} A_P (T_F - T_P) \\ h_{P-F} = \dfrac{k_F (2 + 0.6 Re_P^{1/2} Pr^{1/3})}{2R_P} \end{cases} \quad (13)$$

where C_d is drag coefficient, and is approximated by $C_d = 24/Re_P$; Re_P is Reynold number of particle, denoted as $2R_P \rho_F |\boldsymbol{u}_F - \boldsymbol{u}_P| / \mu_F$; R_P is particle radius; h_{P-F} is heat convective coefficient based on Ranz-Marshall correction [62]; $Pr = c_P \mu_F / k_F$ and $A_P = 4\pi R_P^2$ are the Prandtl number of fluid phase and particle surface area.

(2) From particle phase to fluid phase:

$$\begin{cases} \boldsymbol{f}_{F-P} = -\dfrac{1}{\Delta t} \sum_{\epsilon} \left(\int_t^{t+\Delta t_\epsilon} \int_{\boldsymbol{V_c}} \delta(\boldsymbol{r} - \boldsymbol{r}_\epsilon) n_\epsilon \mathbf{F}_d dV dt \right) \\ Q_{F-P} = -\dfrac{1}{\Delta t} \sum_{\epsilon} \left(\int_t^{t+\Delta t_\epsilon} \int_{\boldsymbol{V_c}} \delta(\boldsymbol{r} - \boldsymbol{r}_\epsilon) n_\epsilon (q_{P-F} + \mathbf{F}_d) dV dt \right) \end{cases} \quad (14)$$

where Δt and Δt_ϵ is the time-step for the CFD and DEM solver, respectively; the Dirac delta function (δ) filters out particles which are not in the cell $\boldsymbol{V_c}$; n_ϵ indicates the number of particle; Q_{F-P} represents the accumulated particle energy in the cell $\boldsymbol{V_c}$.

The strongest simplification in the current CFD-DEM coupling scheme is the ignorance of the conversion from powder to liquid. In order to approximate the melting process, powder is manually removed from the computational domain when its temperature exceeds liquidus line. Besides, only the powder below the layer thickness can be removed, and those powder

Table 1. Thermophysical properties of Ti-6Al-4F employed in the CFD model (symbols in parentheses represent mass fraction averaged variable).

Properties	Symbol	value [unit]
Density (TC_4) [46]	ρ_l	4420 [kg/m^3] ($T < 1268$) 4420 − 0.154 × (T − 300) [kg/m^3] ($T <= 1923$) 3920 − 0.68 × (T − 1923) [kg/m^3] ($T > 1923$)
Solidus line [46]	T_S	1878 [K]
Liquidus line [46]	T_L	1923 [K]
Evaporation line	T_v	3133 [K]
Latent heat of fusion	L_m	2.88×10^5 [J/kg]
Latent heat of evaporation [63]	L_v	9.7×10^6 [J/kg]
Thermal conductivity (TC_4) [46]	k_{F1}	16 [J/(m·K)] (T <= 1923) 32 [J/(m·K)] (T > 1923)
Thermal conductivity (Ar) [41]	(k_{F2})	0.015 [J/(m·K)]
Thermal conductivity (Vapour) [46]		0.05 [J/(m·K)]
Specific heat (TC_4) [63]	c_{F1}	570 [J/(K·kg)] (T <= 1923) 831 [J/(K·kg)] (T > 1923)
Specific heat (Ar) [7]	(c_{F2})	520 [J/(K·kg)]
Specific heat (Vapour) [7]		717 [J/(K·kg)]
Dynamic viscosity (TC_4) [64]	μ_{F1}	0.005 [Pa·s]
Dynamic viscosity (Ar) [65]	(μ_{F2})	2.1e-5 [Pa·s]
Dynamic viscosity (Vapour) [46]		2.4e-4 [Pa·s]
Surface tension coefficient	σ_{F1}	1.5 − 0.00026 (T − 1923) [kg/(s^{2}K)]
Coefficient related to the electrical [55]	ε	0.2
Molar mass (TC_4)	M_{F1}	0.446 [kg/mol]
Molar mass (Ar)	M_{F2}	0.0399 [kg/mol]
Gas diffusivity coefficient [7]	D_{F2}	2×10^{-5} [m^2/s]
Mushy zone number [66]	A_{mush}	1.8×10^8 [m^{-2}]
Heat convection coefficient [67]	h_c	20 [W/m^2]

Table 2. Thermophysical properties of Ti-6Al-4F employed in the DEM model.

Properties	Symbol	value [unit]
Density	ρ_P	4420 [kg/m^3]
Thermal conductivity	k_P	17 [J/(m·K)]
Specific heat	c_P	570 [J/(K·kg)] (T <= 1878) 6970 [J/(K·kg)] (1878 <= T <= 1923) 831 [J/(K·kg)] (T > 1923)
Poisson's ratio	σ	0.34
Young's Modulus	E	107 [GPa]
Static friction coefficient	C_{fs}	0.61
Restitution coefficient	C_r	0.5

above the bed has a capped temperature of 5000 K. Due to this simplification, the specific heat for the powder (c_P) is formulated by:

$$c_P = c_{F1} + \frac{L_m}{T_L - T_S} \tag{15}$$

The adopted values for the thermophysical properties of the materials in the CFD system and DEM system are listed in Tables 1 and 2, respectively.

2.4. Simulation setup and simplification

The computational domain is $0.5 \times 0.5 \times 1$ mm^3, with 500 µm baseplate. The initial powder configuration is established through a standalone DEM simulation, where the powder particle is assumed spherical with a normally distributed diameter range from 15µm to 50µm and a mean value of 30 µm. The obtained layer thickness is 60 µm. Four different laser scan speeds with constant laser power 270 W are the simulation cases for the current study to investigate the role of laser scan speed, as Table 3 shows.

The adaptive meshing grid is applied near the gas-metal interface in addition to the slip velocity boundary, to prevent non-physical phenomena. This approach has been found more effective by the authors than using the slip velocity boundary alone. Given various grid size that have been used in literatures, including 8µm [68], 6 µm [69], 5 µm [64,70,71], 2.5 µm [28,72], 2 µm [7], and 1.5 µm [73], four levels of mesh refinement is employed in the present study, with the maximum of 20 µm for basic size and minimum of 1.25 µm near the gas-metal interface. Besides, 5 µm is for vapour region, and 10 µm for transition. The adaptive meshing is depicted in Figure 1(a).

It should be noted that the current model builds upon three key simplifications: (1) The conversion from particle to fluid is ignored; (2) The laser heat source applies to both the particle and fluid; (3) The 'powder-cohesion' is not considered. Figure 1(b) schematically illustrates the implementation of laser heat source. The amount of heat applied on the ith and kth particle are $f(r_P^i, D_i)$ and $f(r_P^k, D_k)$, respectively. Note that particle heat source in Eq. (9) only applies within the laser spot range, thus two particles P_i and P_k are affected. On the other way, the laser heat source applied to the fluid phase still follows Eq. (5). The volume fraction gradient of the fluid is used to derive the components of the normal vector at the gas-metal interface, expressed by $\mathbf{n} = \mathbf{n_x} + \mathbf{n_y}$. Thus, the incident angle could be represented by $\cos^{-1}\left(\frac{\mathbf{n_y}}{\mathbf{n}}\right)$. The computational framework is built upon the commercial software StarCCM+ solver [66], and the workflow chart between the CFD system and DEM system is schematically illustrated in Figure 1(c). The computation for the 0.3 m/s case, in which the laser scans for 1 ms takes approximately 100 h on a personal computer equipped with an Intel i9-10900 K CPU. It is also worth mentioned that a mesh convergence test was conducted to ensure the model is not sensitive to mesh variations.

Table 3. Four simulation cases employed in the current study.

–	case 1	case 2	case 3	case 4
Laser scan speed	0.3 m/s	0.5 m/s	0.7 m/s	0.9 m/s

3. Results

3.1. Vapour variation phases

A randomly captured snapshot of the vapour profile typically falls into two distinct phases, as shown in Figure 2, which occur consecutively, referred to as the 'initialization phase' and 'processing phase'. The vapour profile from the simulation is visualised using three velocity iso-surfaces, represented by 20 m/s (pink), 50 m/s (yellow), and 100 m/s (grey), respectively. The characteristics of these two phases are as follows:

(1) Initialisation phase:

At the onset of vapour ejection, different laser scan speeds exhibit a similar pattern, as shown in Figure 2(a)–(d). Metal vapour is triggered at approximately 10 µs due to evaporation, flowing continuously upwards. The vapour velocity reaches its maximum at the centre of laser spot, exceeding 100 m/s.

(2) Processing phase:

After the laser has scanned a certain distance, vapour enters the 'processing state', which represents the normal state during LPBF process. As displayed in Figure 2(a')–(d'), the vapour profile inclines. A clear relationship can be observed between laser scan speed and the vapour flow direction, where the latter is described as the vapour flow angle (VFA). Specifically, VFA is the angle between the laser scan direction and the vapour ejection direction, denoted as, θ_1, θ_2, θ_3, and θ_4, respectively. With an elevation in laser scan speed, the VFA also increases, shifting from an acute angle to an obtuse one.

Three different vapour patterns can be observed in 'processing phase', including suppression, interruption and continuity, which are dependent on the laser scan speed. These three patterns agree well with the

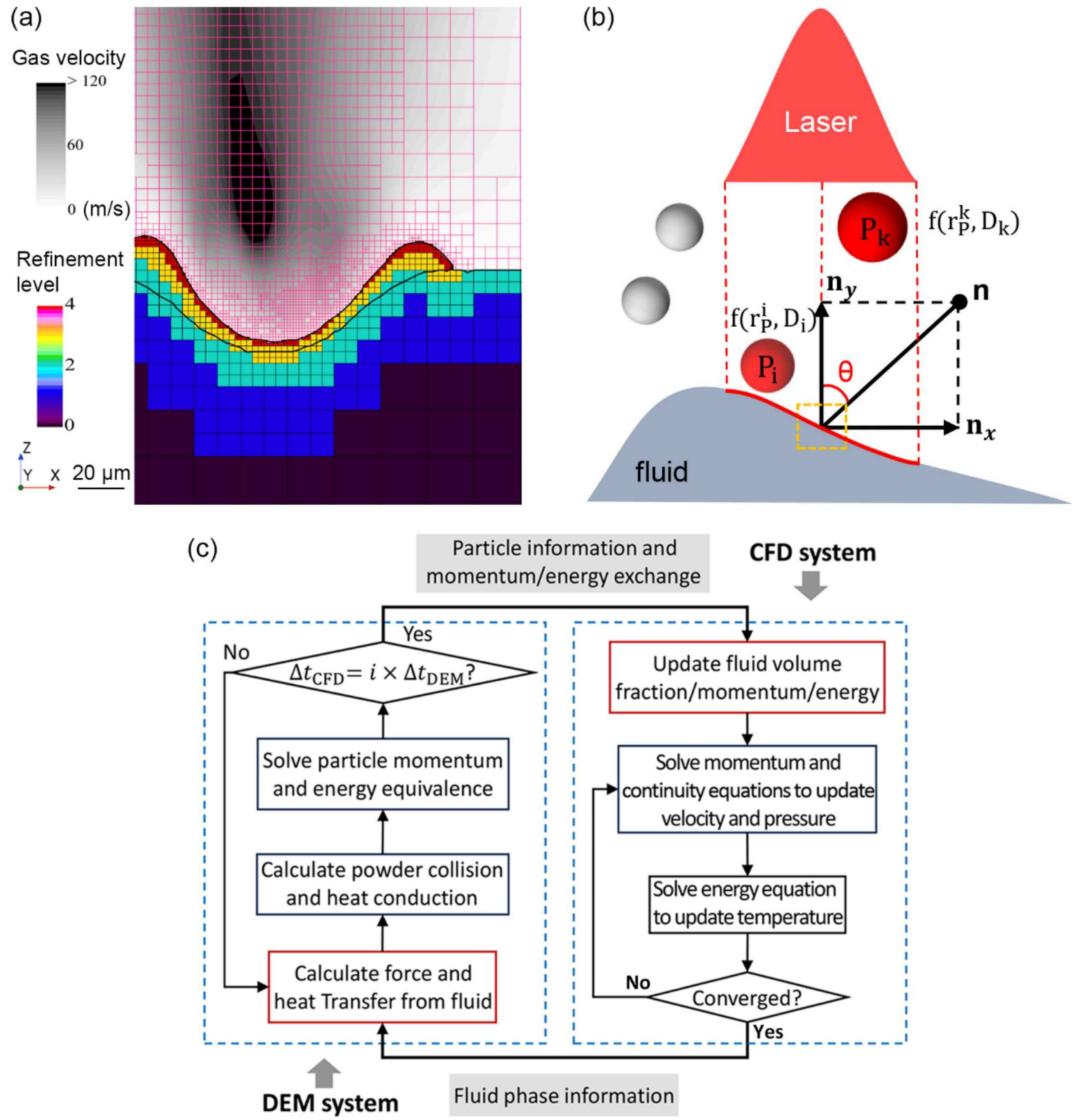

Figure 1. (a) Four levels of adaptive meshing grids used in the simulation with 20 μm for the maximum grid size and 1.25 μm for the minimum grid size. (b) Implementation of laser heat source. (c) Workflow diagram for the CFD-DEM coupled model.

experimental observations by Bitharas et al. [17], as shown in Figure 2(e), (f) and (g). They reported that vapour could consecutively transition through three stages, i.e. stage I, II, and III, subject to exceeding specific energy input threshold, which is met by 0.3 m/s case in the present study (entering stage III). At laser scan speeds of 0.5 and 0.7 m/s, the 50 m/s iso-surface is momentarily disrupted, while the 20 m/s iso-surface remains unaffected (entering stage II). In contrast, the vapour profile at 0.9 m/s always keeps continuous (staying at stage I). The two phases of metal vapour can be validated via the experiments by Zheng et al. [74], and is shown in Figure 2(i). It demonstrates that regardless of the processing parameters, vapour initially ejects vertically from the powder bed and inclines as the process continues. Besides, they noted that vapour could oscillate and may exhibit a periodical pattern. Figure 2(j) was the experiments conducted by Wang et al. [19], where the relationship between scan speed and VFA can be validated. The supplementary video

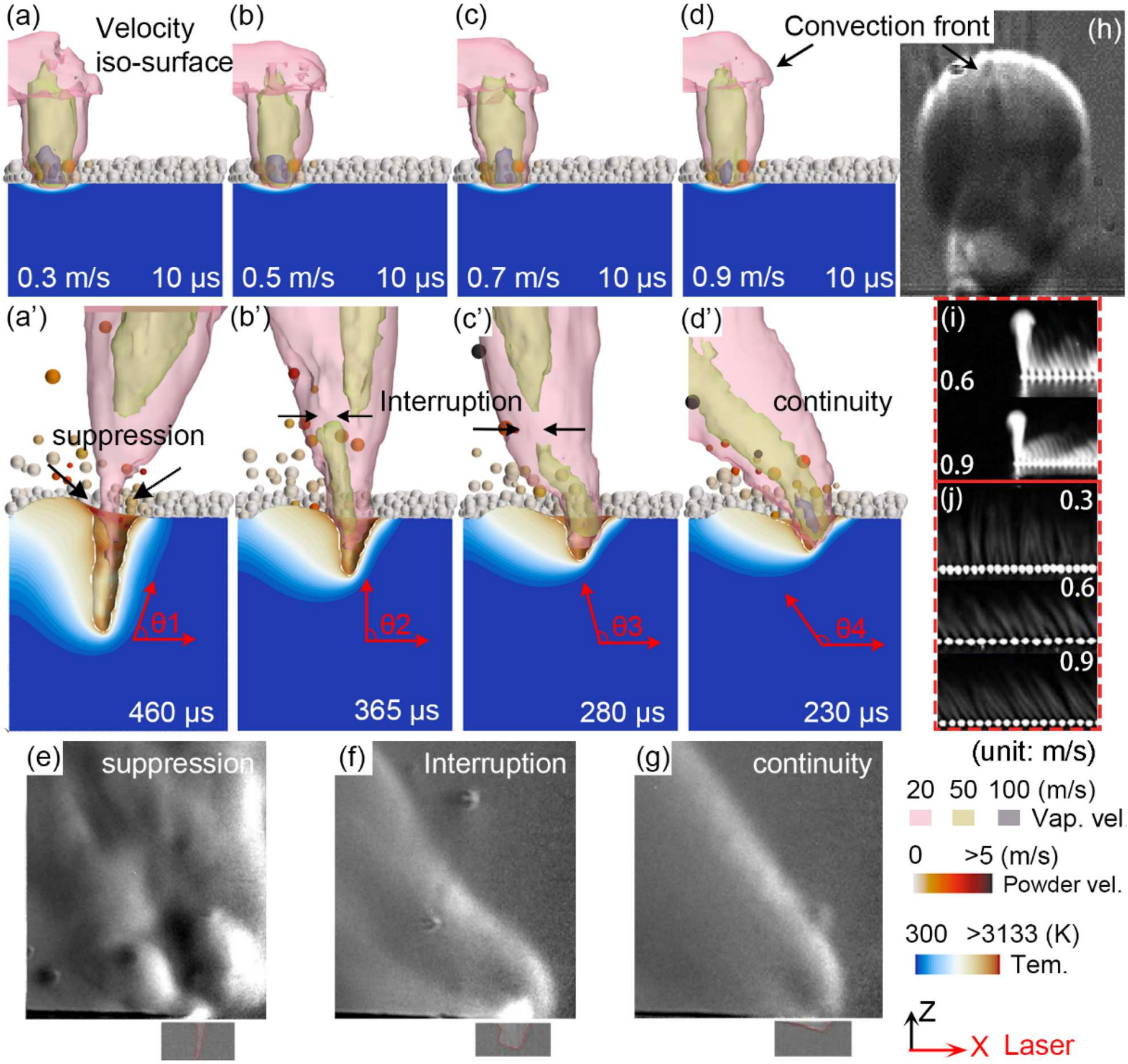

Figure 2. Two vapour phases at different laser scan speeds, including (a)–(d) Initialisation phase, where vapour flows continuously upwards, and (a')–(d') processing phase, where vapour flow angle (VFA) changes positively with laser scan speed; Experimental observations of three vapour patterns in the processing phase [17], including (e) suppression, (f) interruption and (g) continuation; (h) Vapour convection front captured by Schlieren imaging [14]; (i) Experimental validation of two phases [74]; (j) Experimental validation of correlation between the VFA and laser scan speed.

details the complete process of four cases in terms of the evolutions of vapour profile.

3.2. Vapour ejection and oscillation

Vapour can eject from different sides of keyhole wall (referred to as KW hereafter), including front KW, rear KW and bottom KW. These are termed as different vapour ejection modes, clarified as follows:

(1) Front KW mode (F-mode): Vapour predominantly ejects from the front wall of the depression or keyhole, whereas the insignificant amount of vapour emerging from the rear and bottom KW do not affect vapour flow direction.
(2) Rear KW mode (R-mode): The amount of vapour that ejects from the rear KW of the depression or keyhole determines or changes the vapour flow direction.
(3) Combined mode (C-mode): Approximately similar amount of vapour ejects from the rear, bottom and front KW.

Figure 3 shows the transition mechanism of vapour ejection modes at laser scan speed of 0.3 m/s from

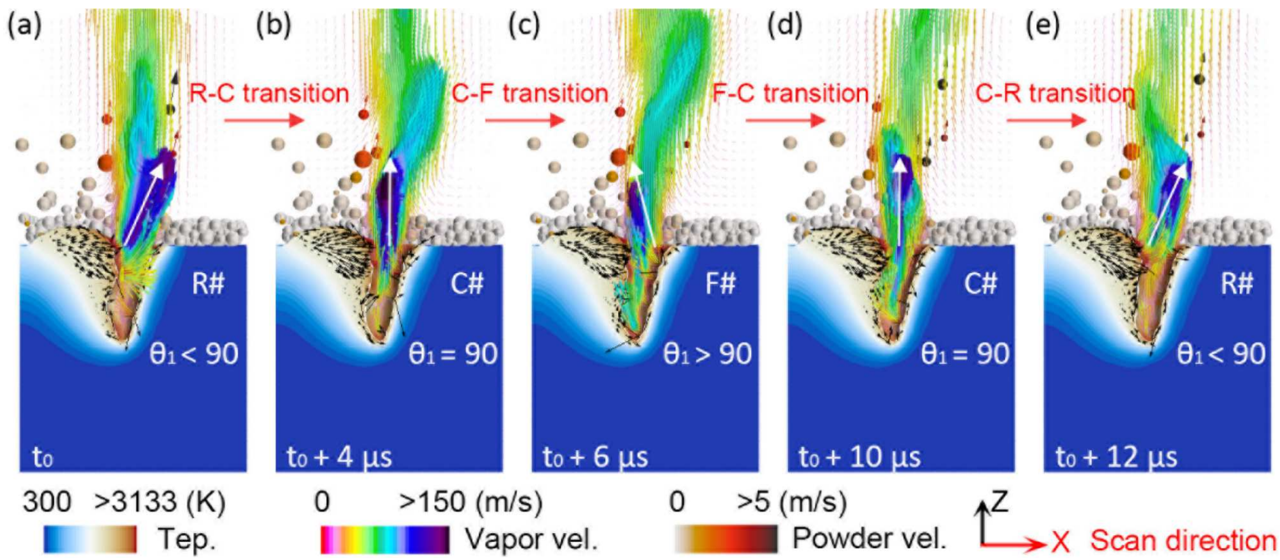

Figure 3. Transition mechanism of vapour ejection mode leads to vapour oscillation behaviours. Viewing from (a) to (e), vapour experiences R-C-F-C-R ejection mode in sequence.

longitudinal section, where a keyhole is formed. The flow conditions of the melt, vapour and powder are combinedly displayed. It is noticeable that vapour does not eject uniformly from the entire KWs, but one or several specific sites on the KWs. At t0, vapour primarily ejects from the rear KW, manifesting R-mode, and the VFA (θ_1) exhibits less than 90 degrees. Subsequently, a transition from R-mode to C-mode occurs at t0+4 μs with θ_1 approximately vertical. The C-F transition follows and is observed at t0+6 μs, where θ_1 exhibits slight larger than 90 degrees. With laser progressing, C-mode and R-mode could restore at t0+10 μs and t0+12 μs, respectively. In a results, the vapour ejection loops through R-C-F-C-R chain. It should be highlighted here the role of melt flow during the transition. The surface melt tends to flow towards the tail due to the Marangoni force, which competes with the recoil pressure to retain a dynamic balance of keyhole shape. However, the downward melt flow near the KWs could change the vapour ejection site, which repeatedly occurs and vanishes at different locations of the KW. In consequence, the vapour then exhibit oscillation behaviours from a zoom-in view.

As laser scan speed increases, the transition of vapour ejection mode can also be observed, as illustrated in Figure 4. Under these circumstance, F-mode predominates the vapour ejection during laser scanning. For the scan speed of 0.5 and 0.7 m/s (see the first and second rows in Figure 4), R-mode could come into effect, as shown in Figure 4(a2) and (b1). Similar to the case of 0.3 m/s, the transition of vapour ejection mode changes the vapour flow direction, and may lead to vapour interruption, as shown in Figure 4(a3) and (b2). An exception is for 0.9 m/s (see the third row in Figure 4), where no transition occurs. However, as the vapour ejection site can still vary due to melt flow, vapour exhibits oscillation as well. There are supplementary videos provided, showcasing the complete laser scanning process for the four cases. The variations of the vapour ejection site aligns with the swing behaviour monitored during laser welding process [75,76].

3.3. Powder trajectories

The variation in vapour ejection mode leads to vapour oscillation, which can incurs various powder behaviours. The first three rows in Figure 5 illustrates powder trajectories at different laser scan speeds from transverse, longitudinal and top view, respectively. Figure 5(f) delineates the powder and its flow direction at the same time. The selected snapshots are captured when laser stays at the same position. Four types of powder trajectories (spatter) can be categorised into follows:

(1) Main trajectory: Driven towards and then moving alongside vapour flow direction, encircled by green dotted line; this is commonly known as powder entrainment pattern [77].
(2) Type I: Powder that flows laterally, marked by blue dotted rectangles;
(3) Type II: Powder that deviates from the main trajectories, marked by blue dotted circles;
(4) Type III: Powder that flows against the main powder trajectories, marked by blue arrows;

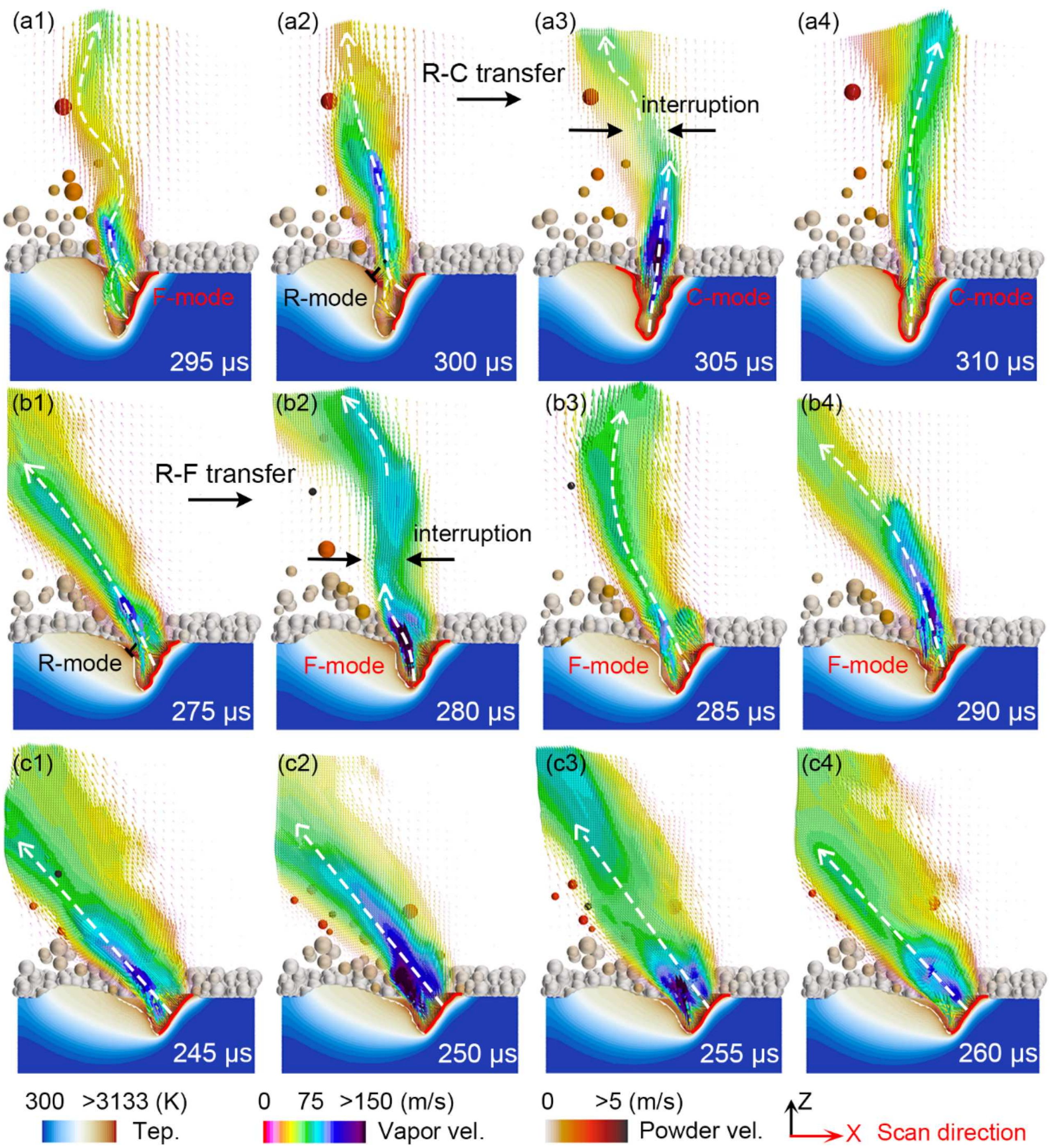

Figure 4. Vapour oscillation at different laser scan speeds: (a1)–(d1) 0.5 m/s, (b1)–(b4) 0.7 m/s, and (c1)–(c4) 0.9 m/s (Partial baseplate is displayed for better visualisation).

At scan speed of 0.3 m/s, the most chaotic powder trajectories are produced, and all types of spatters can be observed, as depicted in Figure 5(a3). With scan speed increasing to 0.5 m/s, the chaotic extent of powder trajectory improves whereas Type I (lateral) spatter can be commonly seen, as Figure 5(b1)–(b3) illustrate. With laser scan speed further increased to 0.7 m/s, vapour constrains powder movement largely towards the vapour flow direction (see Figure 5(c1)–(c3)). In this case, type III spatter may re-occur, exhibiting opposite to the main trajectory. With scan speed elevated to 0.9 m/s (see Figure 5(d1)–(d3)), both the number of type II and type III spatter increase, as shown in Figure 5(d2). It can also be seen from Figure 5(f) that as laser scan increases, the number of spatter decreases. However, powder coalescent may occur as the constrain

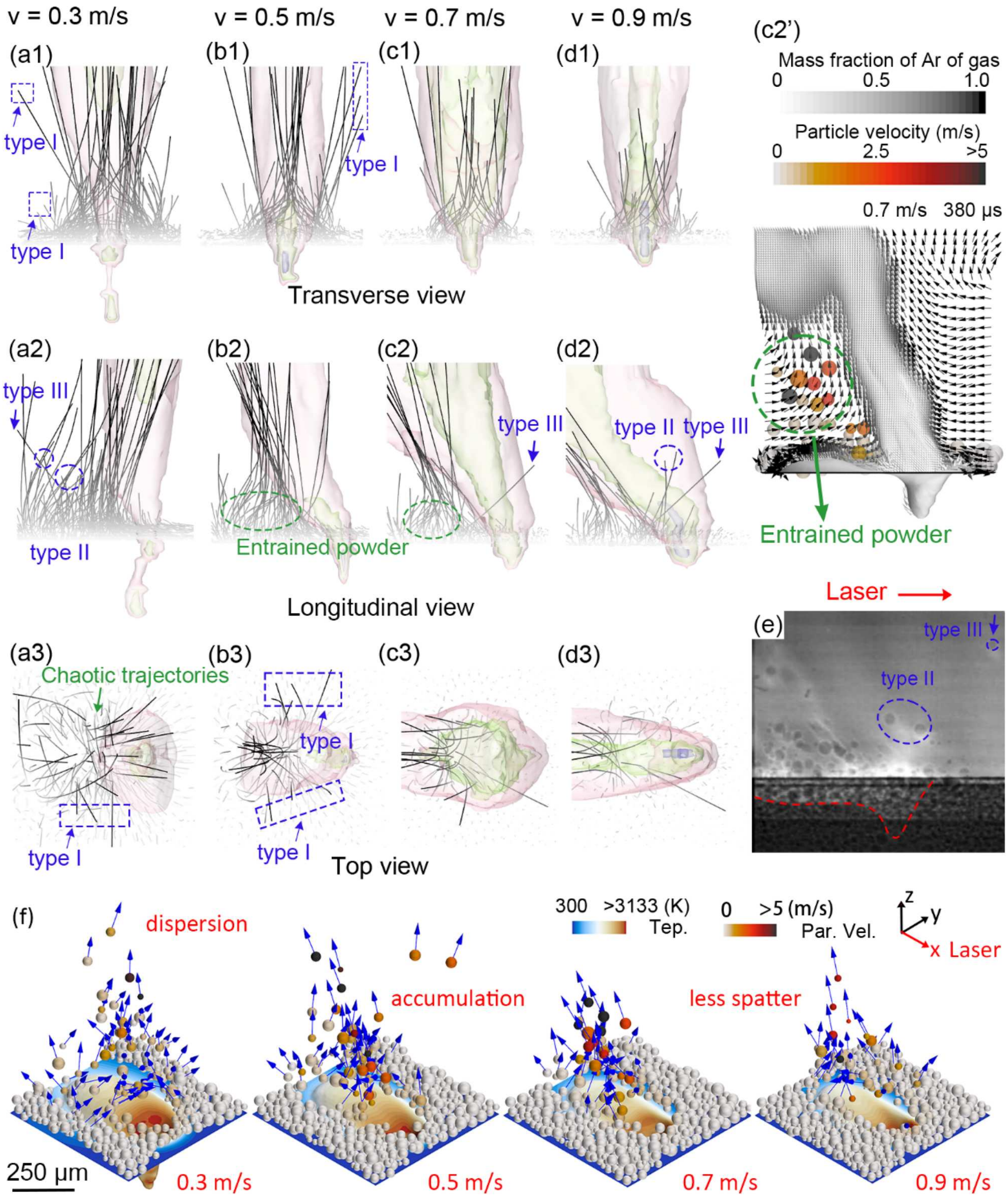

Figure 5. Powder trajectories generated at different laser scan speeds from (a1) to (d1) Transverse view and (a2)–(d2) Longitudinal view. (c2′) Magnified display of the entrained shielding gas for (c2). (a3)–(d3) Top view of powder trajectories. (e) Synchrotron x-ray imaging capturing escape powder [17]. (f) Powder spatter condition from a iso-metric view.

effect of vapour increases due to the increased laser scan speed, shown in 0.5 m/s. This may results in the tendency for agglomerate formation since powder spatter becomes less dispersed. On the other hand, the further elevated scan speed, as shown in 0.7 m/ and 0.9 m/s, inversely decrease the agglomerate tendency.

The resistance effect against the constrain of metal vapour is represented by type II and type III powder.

This is attributed to the decreased energy input as scan speed increases, preventing powder from merging with the melt pool timely. Nonetheless, type II powder is expected to be driven toward the vapour flow direction when the laser passes nearby. Both of these two spatter types can be inspected using synchrotron x-ray imaging [17], as shown in Figure 5(e). It is noted in Figure 5(c2′) that a counter-clockwise vortex flow composed of shielding gas, i.e. argon, forms on the left side of the metal vapour. This is a long-standing recognised entrainment pattern based on the Bernoulli effect [21,78,79], and is often schematically shown in literatures. While this recognition is generally true, it is hard to explain the occurrence of type II and type III spatter (see Figure 5(e)). Affected by both metal vapour and shielding gas, which are closely linked with the melt pool evolution, the powder trajectories should also be interconnected with these factors.

4. Discussion

4.1. Locally intensified pressure

In a previous study where the stationary laser was adopted [80], the fluctuations of metal vapour occurs alongside the augmentation of the melt pool depression, and becomes pronounced with the formation of a keyhole. This is because that the laser absorptivity is highly dependent of the laser incident angle. Laser absorptivity can abruptly increases at the perturbed gas-melt interface. As a result, both keyhole necking (see Figure 6(a)–(a′)) under stationary laser, and keyhole protrusion [81] (see Figure 6(b)–(b′)) under moving laser facilitate metal evaporation.

Because of instant metal evaporation occurring on the keyhole protrusion, the produced metal vapour exerts a large locally intensified pressured (termed as LIP thereafter) on the KW. Vapour predominately ejects from the LIP site regardless of the laser intensity distribution, as shown in Figure 6(c). Here, the melt pool surface (walls of depression or keyhole) can be half divided by laser beam axis, as the vertical dotted line indicate. In the case of LIP site appearing on the rear KW in Figure 6(c), the average recoil pressure incurred by the vapour on the rear KW, denoted as $\overline{RP}$, can transiently elevates. On the other hand, the average recoil pressure on the front KW, denoted as front pressure ($\overline{FP}$), remains unaffected. Several studies have also underscored that melt evaporation could be confined to localised sites on the KW. Pang et al. [76] reported that ‘complex multiple directions vapor’ could be produced by local evaporation. Zhao et al. [82] observed that such local evaporation could induce ‘bulk explosion’ on the KWs. The LIP can significantly exceeds the atmospheric pressure (101,325 Pa) and can force the protrusion to merge back into the melt pool.

4.2. Melt-vapour correlation

Figure 7 illustrates the absolute pressure that the melt pool surface receives at scan speed of 0.5 m/s and its transient variation within 50 μs. A red dotted vertical line in each sub-figure represents the position of laser

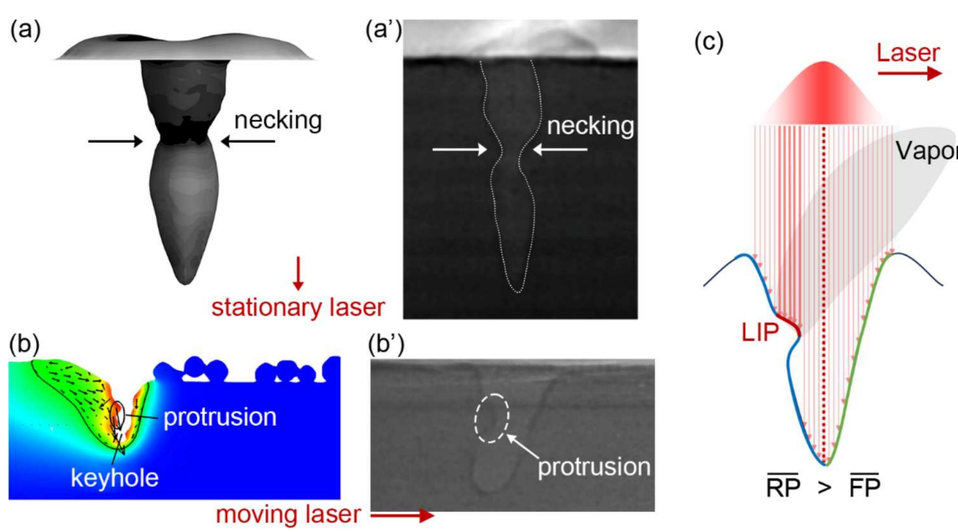

Figure 6. Keyhole necking monitored by (a) simulation [80] and (a′) experiment [17] under stationary laser, and keyhole protrusion monitored by (b) simulation [28] and (b′) experiment [81] under moving laser. (c) Schematic of the production of locally intensified pressure (LIP) site.

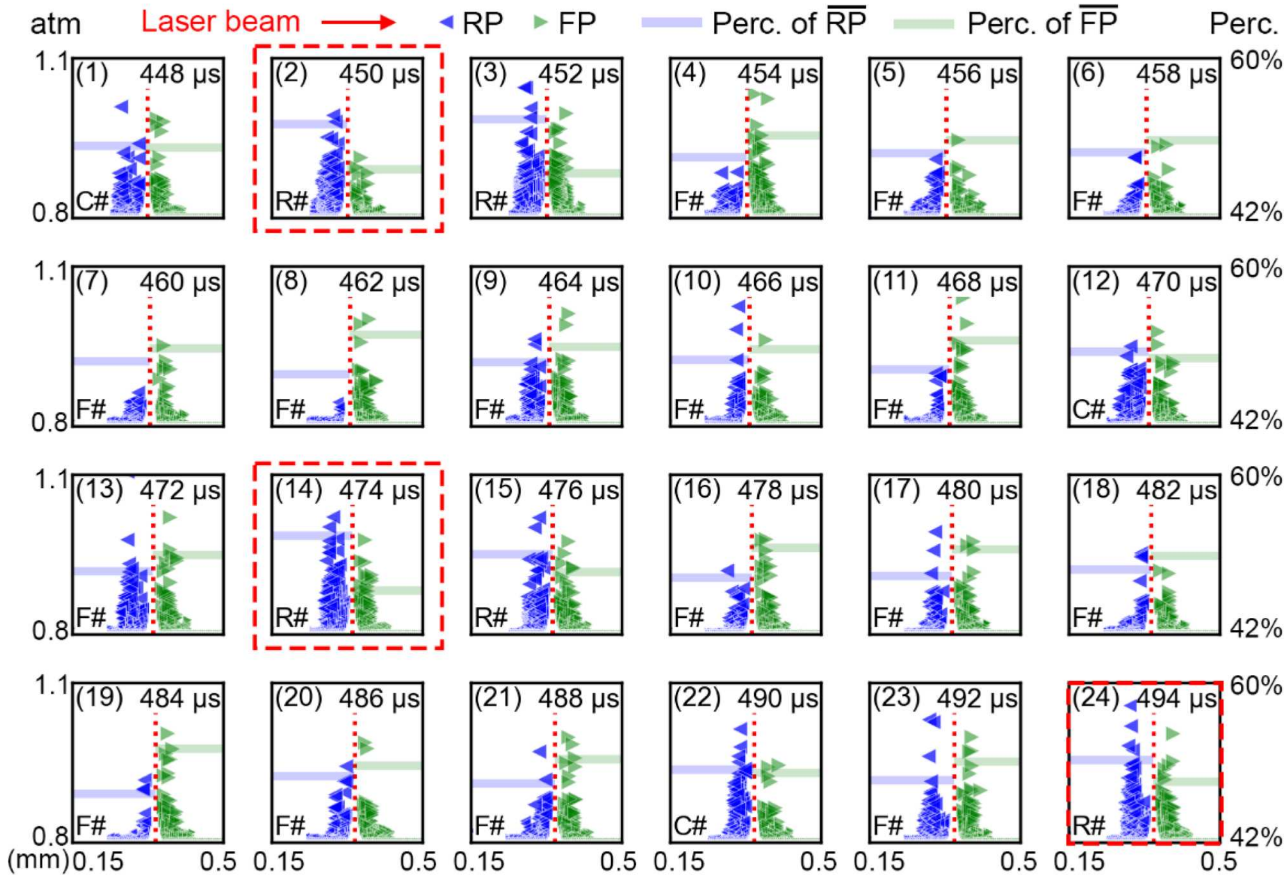

Figure 7. Evolutions of vapour ejection mode indicated by the absolute pressure on the KWs. Snapshots are captured with 2 μs interval, and only the values over 1 atm are displayed.

beam axis. The magnitude of the rear pressure and front pressure are denoted by blue and green triangle marker, respectively. The left and right horizontal solid lines represent the percentage of the magnitude of the averaged rear and front pressure, expressed as:

$$P_R/P_F = [\text{Percentage of } \overline{RP}/\overline{FP}] = \frac{\overline{RP}/\overline{FP}}{\overline{RP}+\overline{FP}}$$

Where $\overline{RP}$ and $\overline{FP}$ represent the averaged rear pressure and front pressure, respectively. The value for each absolute pressure is interpolated based on 5 μm grid resolution, and only the value larger than 1atm is counted.

It is defined that the R-mode or F-mode of vapour ejection is obtained when $\overline{RP}$ is 0.5% larger or smaller than $\overline{FP}$, respectively. Otherwise, the C-mode is established. In this way, each timeframe in Figure 7 corresponds to a specific vapour ejection mode. At 450 μs (Figure 7(2)), the first R-mode occurs. The first R-F mode transition is observed between 452 μs and 454 μs (Figure 7(3)–(4)). Before the second R-mode recovers at 474 μs (Figure 7(14)), vapour ejection mode is dominated by F-mode, albeit the C-mode could be occasionally probed. The third R-mode recovers at 494 μs (Figure 7(24)). It is noteworthy that vapour repeatedly undergoes R-F(C)-R mode transition, and the duration between two non-consecutive R modes is approximately 20 μs. This also implies an 50 KHz oscillation frequency of the absolute pressure. In a study by Khairallah et al. [83], almost the same oscillation frequency was monitored, and they ascribed the periodicity to the varied laser absorptivity.

It should be stressed that the production of metal vapour is the basic engine to induce transient recoil pressure on the melt surface. The periodicity revealed in the case of 0.5 m/s can also find analogies in other processing conditions. Figure 8 illustrates the variation of percentage of $\overline{RP}$ during the entire laser scanning process at four different scan speeds. Each plot includes an inset displaying a curve fragment of 100 μs at vapour processing phase, and the value for the 'percentage of $\overline{RP}$' is shown on the left axis. As the inset indicates, an obvious periodicity can be probed at scan speed of 0.5 and 0.7 m/s after an incubation period. In addition, a 'scan speed-frequency' trend emerges, indicating that higher scan speed results in lower frequency (or higher periodicity). Five peaks are observed at a scan speed of

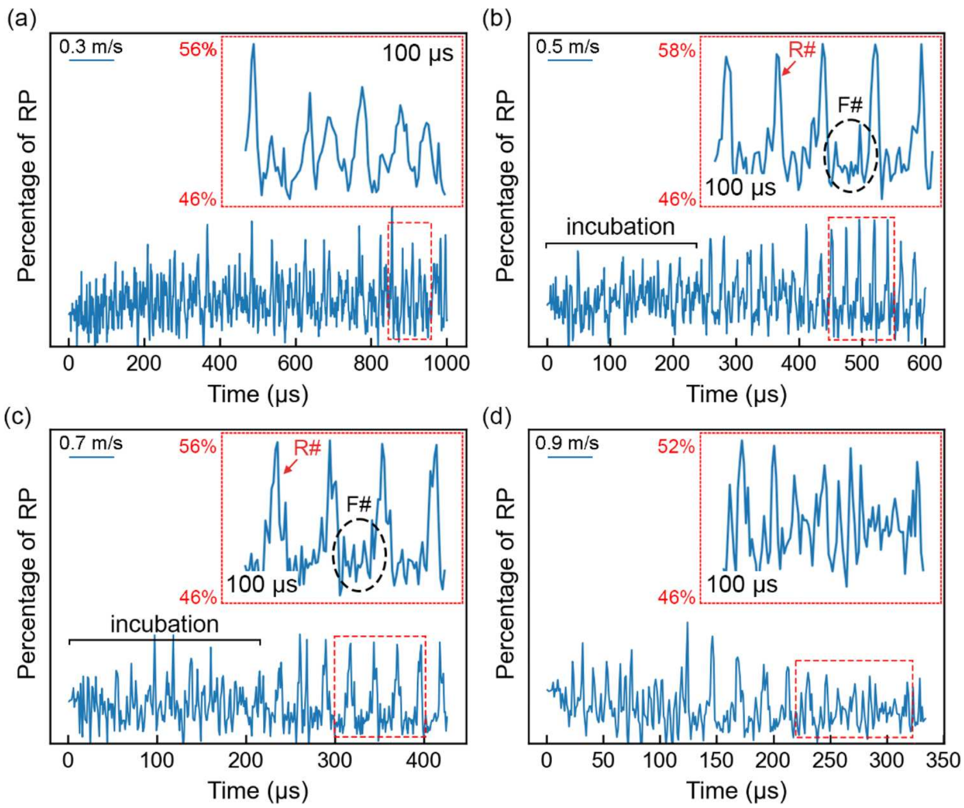

Figure 8. Variation of percentage of averaged absolute pressure on the real KW during the entire laser scan process at scan speed of (a) 0.3 m/s, (b) 0.5 m/s, (c) 0.7 m/s and (d) 0.9 m/s.

0.5 m/s, while four peaks are noted at 0.7 m/s. This trends also applies to 0.3 m/s although with less evident periodicity. The 'scan speed-frequency' trend is ascribed to the fact that the increased laser speed leads to more heat input consumed to drill and create new front KW, thus reducing the occurrence rate for R-mode. On the other hand, the oscillation frequency, i.e. number of peaks, at 0.9 m/s is abnormally high during the entire laser path. Owing to that no R-model comes into play, LIP sites under this circumstance are exclusively generated on the front KW. The LIP sites varies (flows) along the front KW, leading to the fluctuations of the percentage curve (Figure 8(d)). Also note that while the R-mode in the other three cases (0.3 m/s, 0.5 m/s, and 0.7 m/s) is primarily responsible for producing periodicity, the flowing melt of LIP sites manifest as minor fluctuations between consecutive peaks, as the black dotted circle indicates in Figure 8(b) and (c).

4.3. Vapour-argon correlation

As the direct cause of recoil pressure, the involved gases, i.e. vapour and argon, are expected to display oscillatory behaviours as well. This may challenge the traditionally acknowledged Bernoulli induced gas pattern [21]. Figure 9 exhibits the vapour and argon flow conditions at the same timeframes and scan speed to that shown in Figure 7. Powder is manually hidden for a refined visualisation. As cycle I starts, a vortex flow with counter-clockwise swirling direction, labelled as vortex I and marked by red dotted circle, is observed on the left side of vapour. Note that vortex I at 450 μs derives from a previous cycle (448 μs). Subsequently, vortex I elevates and exits the boundary, as shown in Figure 9(2)–(3). Almost simultaneous to cycle I begins, vortex II forms on the right side of vapour with clockwise swirling direction, marked by the black dotted circle. Vortex II also gradually ascends along the vapour-argon interface, shown in Figure 9(2)–(5). Before the second R-mode recovers at 474 μs (see Figure 9(14)), a new vortex I forms at 466 μs (see Figure 9(10)), and a new vortex II also recovers at 474 μs. Due to repeat occurrence and absence of the two vortex flows, the powder may experience different directions of drag force at different times. As a consequence, the powder could move against the vapour flow direction, leading to the formation of type II and III trajectory (spatter) as seen in Figure 5. According to a study by Nassar et al. [84], the escaped spatter could evolve into residual

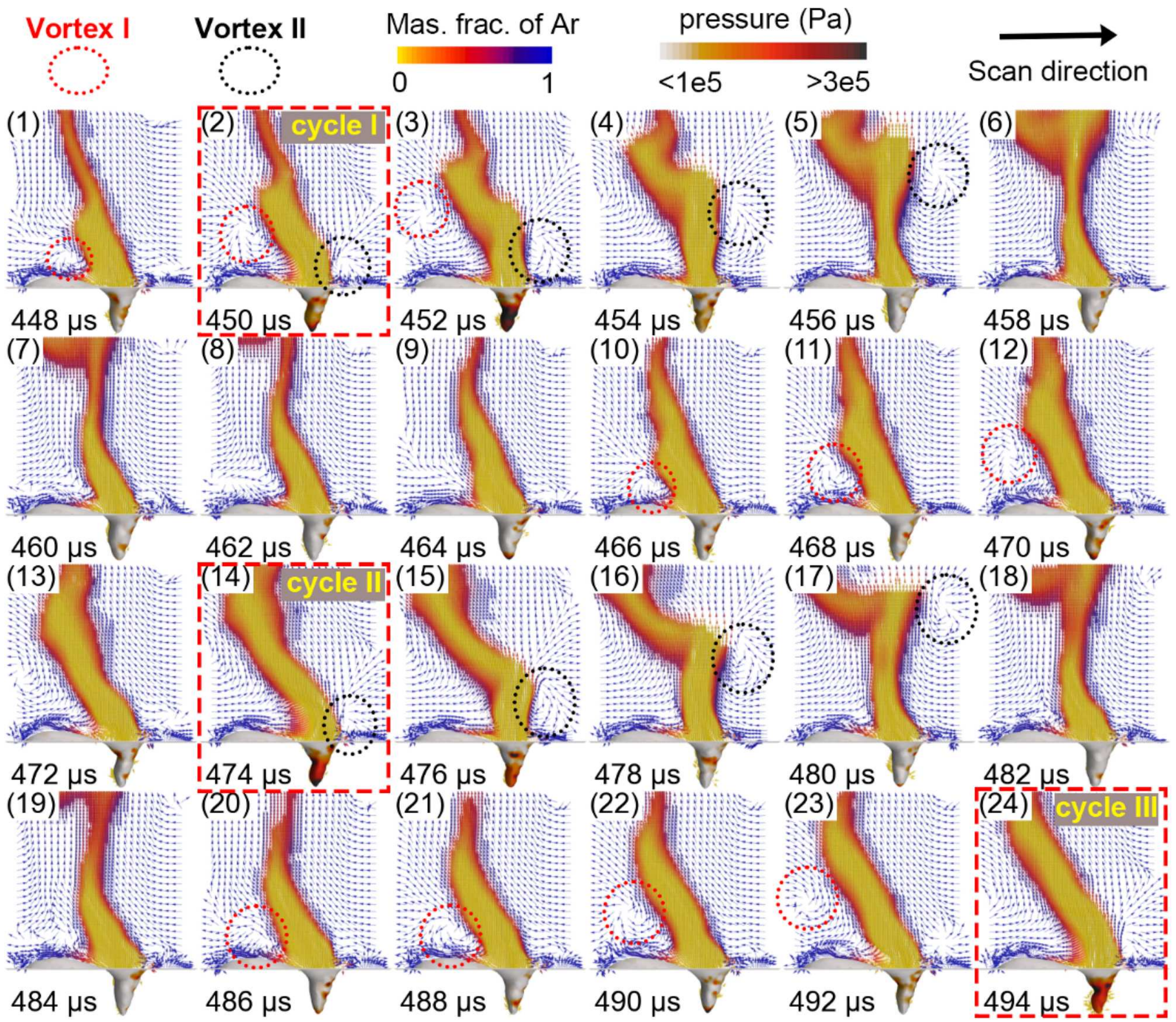

Figure 9. Evolutions of vapour-argon flow pattern at 0.5 m/s, characterised by two vortex flows with opposite swirling directions. Snapshots are captured at the same timeframes to Figure 7.

spatter waste on the scanned area, deteriorating the quality of subsequent tracks.

To quantify the two vortex flows, Figure 10 exhibits the x-component velocity (X-Velocity) versus the laser scan direction from the longitudinal section at different heights (Z-Position). Snapshots are also captured with the same timeframes to that of Figure 9. At current scan speed, where the VFA is equal or less than 90 degrees, vapour only exhibits non-positive x-component velocity, whereas the argon velocity can be both positive and negative. On the left side of laser axis, the maximum positive x-velocity (see Z = 550 μm), i.e. argon velocity, coincides with the start of each cycle, (see Z = 550 μm in Figure 10(2), (14) and (24)), and experiences decrease and consecutively increase within one cycle. Simultaneously, the x-component velocity of vapour reaches its minimum, as Z = 550 μm shows at the laser axis.

Since the line of Z = 550 μm is within the height of powder layer, argon can directly impact powder bed. As a result, the gas momentum can thus be continuously transferred and accumulated in powder during laser scans along the +x direction, allowing the powder to overcome internal resistance and move in the direction of the laser. This in turn triggers a powder entrainment pattern, as shown in Figure 5(b2) and (c2). On the other hand, all the curve fragments on the right side of laser axis present argon velocity. These curve fragments begin to oscillate at the onset of each cycle in the form of vortex II. However, the momentum generated by vortex II is scarcely transferred to the powder ahead due to the solid–liquid phase change (melting) of the powder. This is also reflected by the rapid diminishment of positive x-velocity. As a consequence, the subtle momentum transferred to the powder dissipates

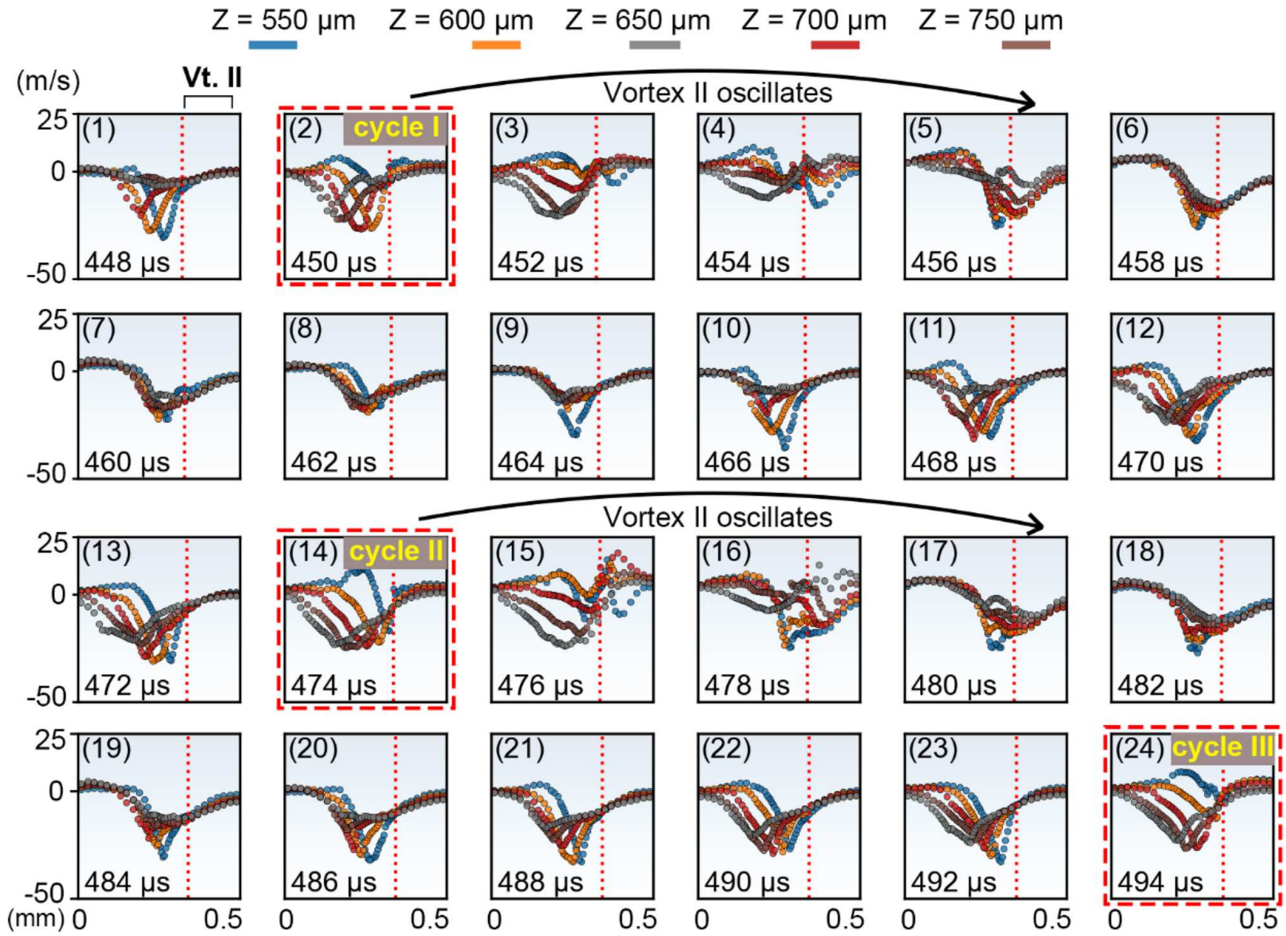

Figure 10. Variation of the distribution of X component gas velocity on the longitudinal section at different heights (Z position). Snapshots are captured at the same time frames to Figures 7 and 9.

in two ways: by forming a liquid micro-jet, as observed by Sonny et al. [85] or by occasionally forming type II and type III powder spatter (see Figure 5).

As for the case of 0.3 m/s, Figure 11 presents four representative argon-vapour flow scenarios from a longitudinal section. Under this circumstance, the keyhole dimensions expend, particularly for its depth. This boosts more frequent and provides broader areas for the production of LIP sites. As a consequence, the vapour ejection mode can shift among R-mode, C-mode and F-modes with no determined sequence. The resultant two vortex flows can occur and evolve either simultaneously (Figure 11(a)), sequentially (Figure 11(b)), or separately (Figure 11(c,d)), leading to complex momentum transfer from gas to powder. This complexity is the major reason why powder trajectories exhibit the most chaotic in Figure 5.

4.4. Gas-powder correlation

It can be anticipated that the powder should exhibit analogous oscillatory behaviours to vapour and argon since they directly contact with one another. Although several studies have investigated the gas-powder interaction around LPBF, none have extensively explored their dynamic correlations. It has been reported that powder-related by-products, such as powder spatter [86] and the formation of agglomerates [87], can adversely influence the quality of SLM processed parts. Therefore, the gas-powder interaction mechanisms should be considered a critical factor, yet they remain poorly understood. Figure 12 displays isometric view of the powder drag forces and directions induced by gas oscillation at 0.5 m/s. During the process that vapour swings forward within one cycle, for instance from 450 μs to 456 μs in cycle I (see blue arrow), most powder displays positive X-component drag force, which is quantitatively illustrated in Figure 13 at the same timeframes. Conversely, in the process of vapour swinging back, as seen from 456 μs to 474 μs in cycle I, the powder drag force gradually changes direction. A supplementary video is also provided for the four cases regarding the gas-powder interaction.

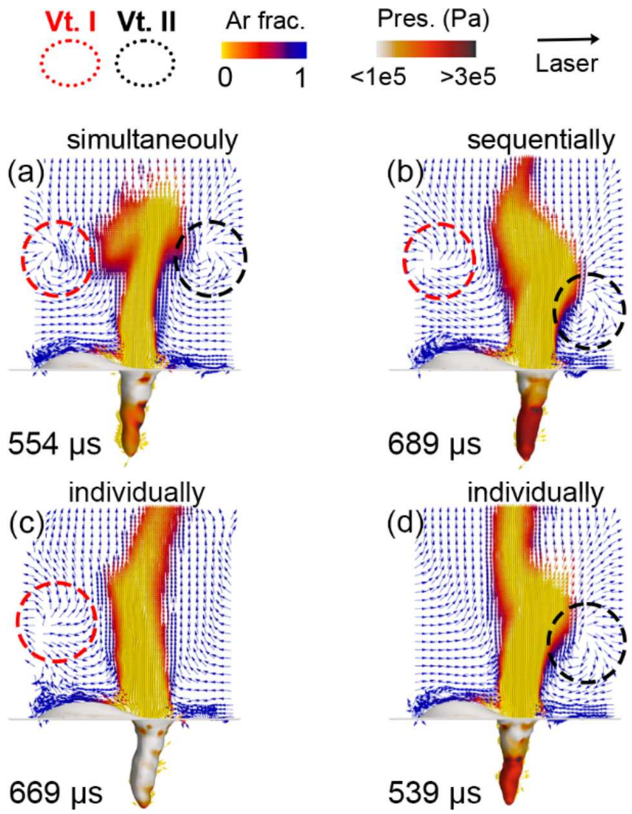

Figure 11. Vapour-argon flow patterns at laser scan speed of 0.3 m/s. The occurrence of two vortex flows can be (a) Simultaneous, (b) sequential, or (c)–(d) separate.

Figure 13 depicts the x-component drag force that all the powder received versus the X direction at scan speed of 0.5 m/s, with same timeframes to that in Figures 7, 9 and 10. On the left side of laser beam, the number of powder with positive X-drag force gradually increases from a moment in one prior cycle (such as 470 μs in cycle I) to the maximum in the next cycle (such as 478 μs in cycle II). This observation is consistent with the discussion in section 4.3. The momentum transferred from vortex I to the powder from argon on the left side of laser can accumulate during laser swings forward. In contrast, the positive X-drag force on the right side of laser beam quickly diminishes within one cycle and the momentum transferred from vortex II to the powder is almost negligible.

In addition, the percentage of powder with positive X drag force is plotted in Figure 14. The curves for the other three laser scan speeds during the laser journey are also displayed. Similar to Figure 8, the inset of each subplot spans a 100 μs period. A periodicity emerges for the first three cases, with two key aspects to note:

(a) At the onset of the laser, the percentage of positive X drag force is extremely high in all four cases. This indicates that powder experiences a strong, unidirectional drag force during the vapour ‘initialization phase’.
(b) Although the peak height may vary, the periodicity of the powder drag force is clear, particular for the case of 0.5 and 0.7 m/s after an incubation period. The periodicity displayed in Figure 14 is equal to that shown in Figure 8, approximately 20 μs (50 KHz) and 25 μs (40 KHz), respectively. The case of 0.3 m/s experiences the smallest periodicity, ranging approximately 12.5 μs to 16.7 μs (60 KHz to 80 KHz).

The oscillation in the melt-vapour interaction (Figure 8) is driven by the variations of LIP sites, which emphasises the critical role of LIP in affecting vapour behaviours, which in turn influences the melt pool stability and morphology. On the other hand, the periodicity inspected in Figure 14 arises from gas-induced powder drag forces. These two oscillatory characteristics are inherently connected, linking the dynamic behaviours of the melt pool, gas, and powder spatter.

The variations in respect of the melt-gas-powder oscillations at 0.5 and 0.7 m/s are shown in Figure 15. A complete in-process evolutions are provided in the supplementary videos. Under these circumstances, oscillations could convert into periodic behaviours, where the variations of LIP and drag force showcases a synchronisation. This situation could establish highly connections with other studies. Huang et al. [88] also reported a synchronisation behaviour between vapour velocity and melt pool dynamics during laser welding process, and attribute these variations to local evaporation. This synchronisation highlights a critical feedback loop, where vapour generated by local evaporation influences melt pool behaviour, which in turn alters vapour characteristics – a cycle that can significantly affect the process stability and part quality. There are also several studies reporting oscillatory behaviours concerning the melt pool in the context of LPBF process [89]. While most of these studies focus on the melt pool, the present one extends these observations by providing a more comprehensive understanding and visualisation of the underlying mechanisms correlating the melt-gas-powder system with processing parameters.

4.5. Insight for process optimisation

As is widely recognised, excessively low or high energy input is undesired in the LPBF process. In this study, laser speeds of 0.5 and 0.7 m/s, which represent intermediate settings, result in stable periodicity and may therefore be more favourable for reducing defects.

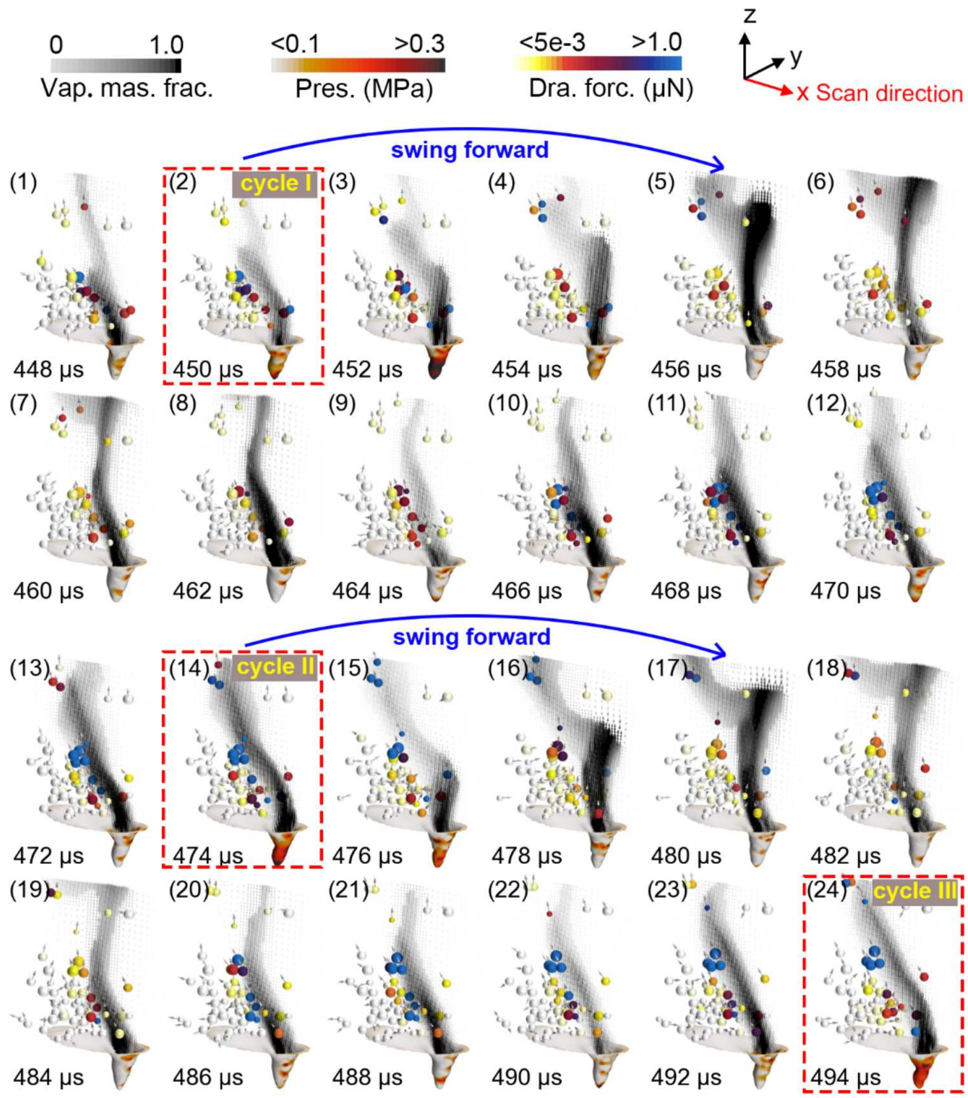

Figure 12. Evolutions of combined powder drag force, LIP on the keyhole wall and vapour mass fraction. For better visualisation, only the powder above layer thickness (60 μm) is displayed.

Support evidence can be found in Khairallah et al. [83], who reported a tendency for pore generation when stable periodicity was disrupted. Additionally, a regular oscillation periodicity may decrease the likelihood of forming agglomerate, as it allows spatter to move in a more organised manner. This regularity aids in controlling the dispersal of spatter and reducing the accumulation of defects, thereby enhancing the quality of the finished products. Moreover, all types of spatter are detrimental to fabricating defect-lean LPBF parts, and are expected to be removed by the cross-blow gas. However, it has been reported that the cross-blow gas can only affect the laser plume when it reaches a sufficient height (on the centimetre scale) [90]. From this perspective, a vertical vapour flow direction (VFA approximately equals 90 degree), as seen with a laser scan speed of 0.5 m/s, may be more advantageous for spatter removal. It is also worth mentioning that within the scope of the LPBF process, research has largely focused on real-time monitoring techniques, such as acoustic emission (AE) detection, with the hypothesis that different metallurgical defects can generate unique spectral of oscillation frequencies [91,92]. While the sensor data may overlook the underlying mechanism [93], the oscillatory behaviours identified in this study through physics-based simulation provide a foundation for using frequency-sensitive techniques in real-time quality monitoring of process anomalies.

4.6. Future way

Although correlations have been established regarding melt-vapour, vapour-argon and gas-powder, further details should be explored as the current model might

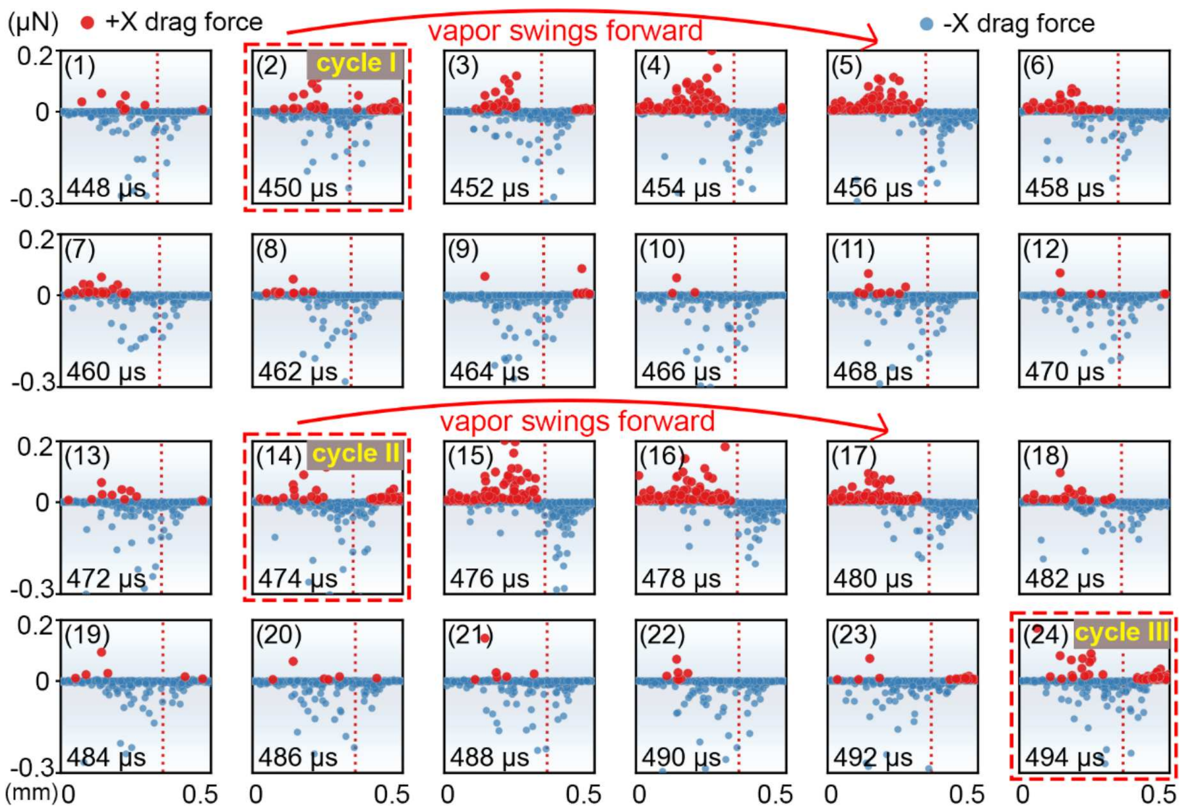

Figure 13. Variation of the X component powder drag force along the longitudinal direction with the same timeframes used in Figures 7, 9, 10, and 12.

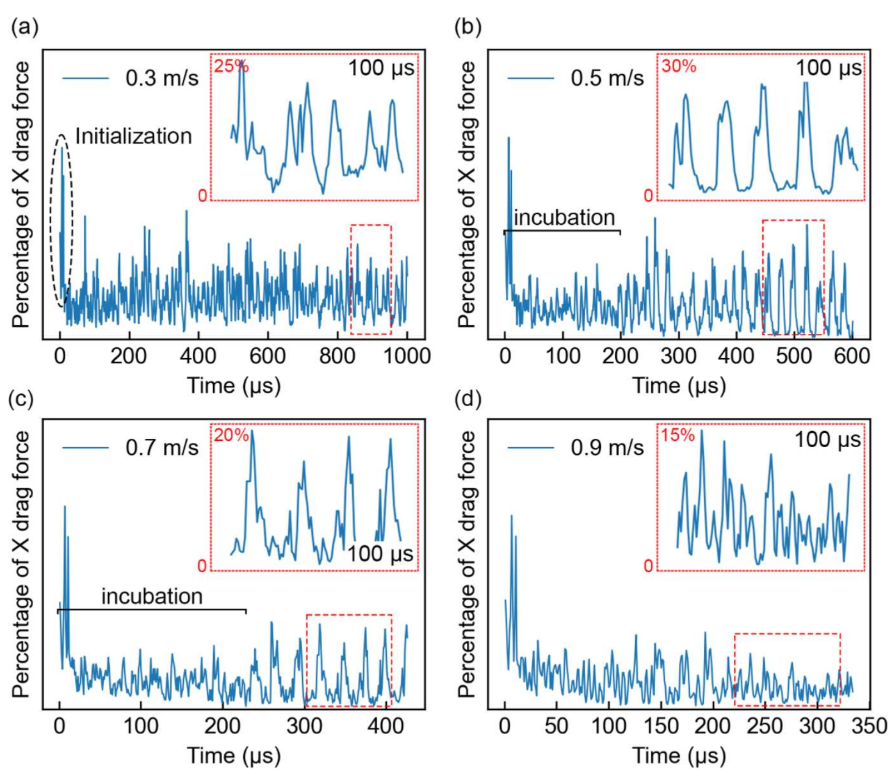

Figure 14. Percentages of the powder receiving +X component drag force during the entire laser scanning process at different scan speeds, including (a) 0.3 m/s, (b) 0.5 m/s, (c) 0.7 m/s and (d) 0.9 m/s.

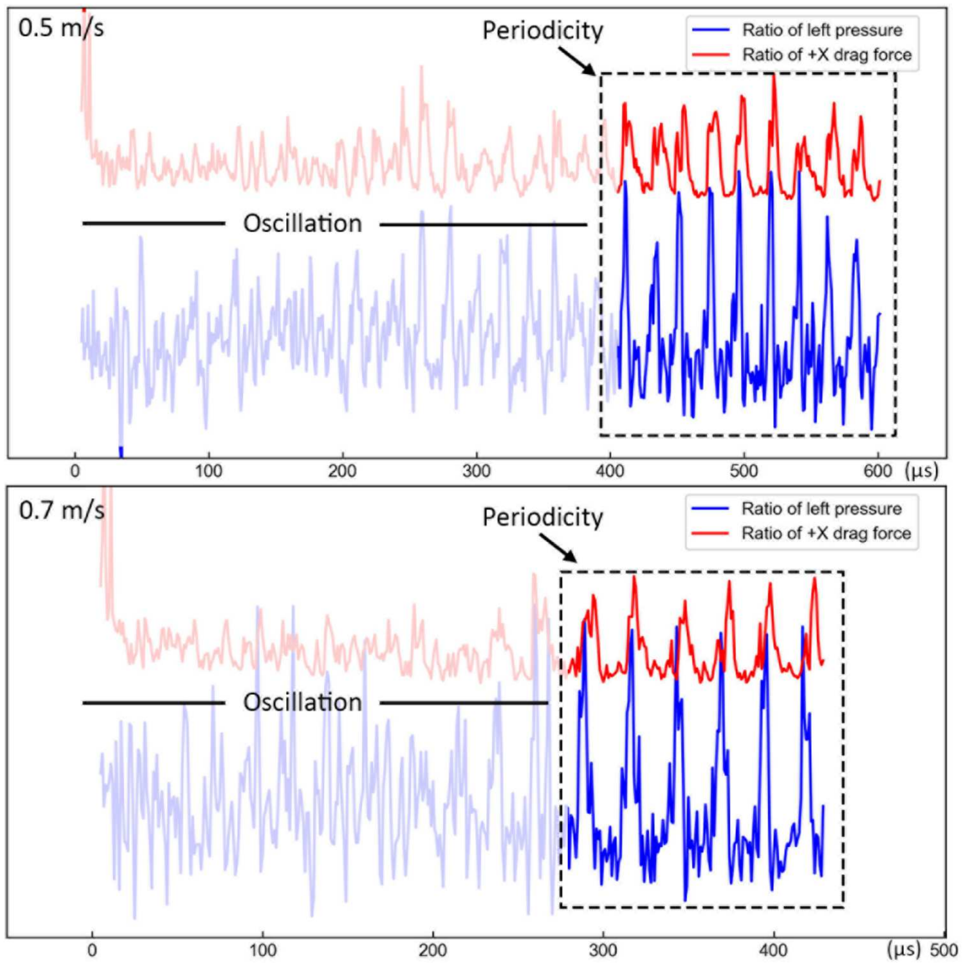

Figure 15. Variations of locally intensified pressure (LIP) and drag force with laser scanning, where the oscillation could evolve into periodic behaviours.

not fully represent realistic LPBF process. For instance, no direct linkage is established between the melt pool and powder spatter. A recent study [94] employs melt velocity gradient and Marangoni intensity to evaluate spatter intensity, suggesting a potential correlation between these two components. The comprehensive oscillatory nature observed in the melt-gas-powder system also suggests that it may not be convincing enough to assess process stability through a single indicator, such as through a single melt pool model. However, the melt pool behaviour remains crucial because it intimately correlates other critical indicators, including metal vapour, shielding gas, and powder spatter. The follows provide two potential ways for future study.

(1) It would be valuable to incorporate the effects of powder deformation and adhesion between particles, which can further refine the categories of spatter and account for the formation of agglomerates during the LPBF process. Understanding these interactions may help better control and reduction of metallurgical defects in the final product.
(2) Given the complexity and computational constraints of physics-based model, surrogate model can offers significant advantages. Such model should leverage of the information provided by different levels of physics, particularly the three relationships studied. Thus, a multi-fidelity surrogate model can be a choice, which is also a proper way for process optimisation. Several pioneer studies have been conducted [95,96], but none have been integrated with the correlations discussed in the current study.

5. Conclusion

Leveraging of the coupled CFD-DEM model, this study reveals the oscillatory nature beneath the LPBF process involving melt-gas-powder interactions. Many results are reported for the first time and can establish connections with existing literatures. This study diverges from conventional focus that primarily on the individual or partial component, thus providing a much more comprehensive insight into the underlying mechanism of LPBF. Key findings are summarised as follows:

(1) In the LPBF process, metal vapour typically undergoes two distinct phases at varying laser scan speeds. The first is the 'initialization phase', during which vapour ejects vertically and continuously. The second is the 'processing phase', where the vapour flow angle (VFA) shows a positive correlation with laser scan speed. Under this circumstance, fluctuations on the walls of the depression or keyhole create locally intensified pressure (LIP) sites, from which the vapour predominantly ejects
(2) There are three types of oscillations in the LPBF process. The first arises from the periodic variations of LIP sites, which occur on the rear wall of the depression or keyhole under specific processing conditions. The second is simultaneously induced and characterised by the repeated occurrence of two argon vortex flows. The third stems from gas-powder interactions, indicated by the proportion of the +X component of the drag force exerted on the powder.
(3) Only under the intermediate scan speeds the oscillation exhibits stable periodicity, implying a way of assessing process stability via different types of oscillatory behaviours in LPBF. Future way of research could consider establishing surrogate model via integrating different sources of information from different oscillatory behaviours.

Acknowledgement

Special gratitude is owed to Professor Shuo Yin for his invaluable pivotal guidance throughout this study, and to Professor Hui Chen for his insightful comments and expert advice on the modelling aspects of this work.

Disclosure statement

No potential conflict of interest was reported by the author(s).

Funding

The authors acknowledge the financial support from the European Innovation Council Pathfinder Project (grant number 101046835), the China Scholarship Council-E3 Studentship (grant number 202006160011), and the Marie Skłodowska-Curie Actions Postdoctoral Fellowship (grant number 101109931).

Data availability statement

Data that support the findings are given in the figures and tables within the article, and the following link for videos: https://drive.google.com/drive/folders/1PGsi737T-WxE3_auukkUUIvk7bofEZ2A?usp=drive_link.

Authors' contributions

Weihao Yuan: Conceptualisation, Methodology, Software, Formal analysis and investigation, Writing – original draft; **Hui Chen**: Formal analysis, Methodology, Software; **Siyuan Ruan**: Writing – original draft; **Rocco Lupoi**: Funding acquisition; **Shaocong Qin**: Formal analysis, Methodology; **Enyu Guo:** Formal analysis, Methodology; **Jianfeng Wang:** Formal analysis, Funding acquisition; Writing – review and editing. **Shuo Yin**: Supervision, Resources, Funding acquisition, Writing – review and editing.

References

[1] Astm I. ASTM52900-15 standard terminology for additive manufacturing—general principles—terminology. ASTM Int West Conshohocken PA. 2015;3(4):5.
[2] DebRoy T, Wei HL, Zuback JS, et al. Additive manufacturing of metallic components – process, structure and properties. Prog Mater Sci. 2018;92:112–224. doi:10.1016/j.pmatsci.2017.10.001
[3] Guo Q, Zhao C, Escano LI, et al. Transient dynamics of powder spattering in laser powder bed fusion additive manufacturing process revealed by in-situ high-speed high-energy x-ray imaging. Acta Mater. 2018;151:169–180. doi:10.1016/j.actamat.2018.03.036
[4] Qu M, Guo Q, Escano LI, et al. Controlling process instability for defect lean metal additive manufacturing. Nat Commun. 2022;13(1):1079. doi:10.1038/s41467-022-28649-2
[5] Martin AA, Calta NP, Khairallah SA, et al. Dynamics of pore formation during laser powder bed fusion additive manufacturing. Nat Commun. 2019;10(1):1987. doi:10.1038/s41467-019-10009-2
[6] Hojjatzadeh SMH, Parab ND, Yan W, et al. Pore elimination mechanisms during 3D printing of metals. Nat Commun. 2019;10(1):3088. doi:10.1038/s41467-019-10973-9
[7] Gan Z, Kafka OL, Parab N, et al. Universal scaling laws of keyhole stability and porosity in 3D printing of metals. Nat Commun. 2021;12(1):2379. doi:10.1038/s41467-021-22704-0
[8] Huang Y, Fleming TG, Clark SJ, et al. Keyhole fluctuation and pore formation mechanisms during laser powder bed fusion additive manufacturing. Nat Commun. 2022;13(1):1170. doi:10.1038/s41467-022-28694-x
[9] Cunningham R, Zhao C, Parab N, et al. Keyhole threshold and morphology in laser melting revealed by ultrahigh-speed x-ray imaging. Science. 2019;363(6429):849–852. doi:10.1126/science.aav4687
[10] Zhao C, Parab ND, Li XX, et al. Critical instability at moving keyhole tip generates porosity in laser melting. Science. 2020;370(6520):1080. doi:10.1126/science.abd1587
[11] Zhao X, Zhang W, Chen H, et al. Analysis of dynamic characteristics of vapor plume of oscillating laser

welding of SUS301L-HT stainless steel. Opt Laser Technol. 2023;159:108947. doi:10.1016/j.optlastec.2022.108947
[12] Yadroitsev I, Smurov I. Surface morphology in selective laser melting of metal powders. Phys Procedia. 2011;12:264–270. doi:10.1016/j.phpro.2011.03.034
[13] Matthews MJ, Guss G, Khairallah SA, et al. Denudation of metal powder layers in laser powder bed fusion processes. Acta Mater. 2016;114:33–42. doi:10.1016/j.actamat.2016.05.017
[14] Bidare P, Bitharas I, Ward RM, et al. Fluid and particle dynamics in laser powder bed fusion. Acta Mater. 2018;142:107–120. doi:10.1016/j.actamat.2017.09.051
[15] Bidare P, Bitharas I, Ward RM, et al. Laser powder bed fusion in high-pressure atmospheres. Int J Adv Manuf Technol. 2018;99(1-4):543–555. doi:10.1007/s00170-018-2495-7
[16] Yin J, Wang D, Yang L, et al. Correlation between forming quality and spatter dynamics in laser powder bed fusion. Addit Manuf. 2020;31:100958. doi:10.1016/j.addma.2019.100958
[17] Bitharas I, Parab N, Zhao C, et al. The interplay between vapour, liquid, and solid phases in laser powder bed fusion. Nat Commun. 2022;13(1):2959. doi:10.1038/s41467-022-30667-z
[18] Zheng H, Li H, Lang L, et al. Effects of scan speed on vapor plume behavior and spatter generation in laser powder bed fusion additive manufacturing. J Manuf Process. 2018;36:60–67. doi:10.1016/j.jmapro.2018.09.011
[19] Wang Y, Guo W, Xie Y, et al. In-situ monitoring plume, spattering behavior and revealing their relationship with melt flow in laser powder bed fusion of nickel-based superalloy. J Mater Sci Technol. 2024;177:44–58. doi:10.1016/j.jmst.2023.07.068
[20] Zhang Y, Yan W, Peng X, et al. Investigation into the optical emission of features for powder-bed fusion AM process monitoring. Int J Adv Manuf Technol. 2022;121(3-4):2291–2303. doi:10.1007/s00170-022-09414-7
[21] Liu Z, Yang Y, Han C, et al. Effects of gas flow parameters on droplet spatter features and dynamics during large-scale laser powder bed fusion. Mater Des. 2023;225:111534. doi:10.1016/j.matdes.2022.111534
[22] Khairallah SA, Anderson A. Mesoscopic simulation model of selective laser melting of stainless steel powder. J Mater Process Technol. 2014;214(11):2627–2636. doi:10.1016/j.jmatprotec.2014.06.001
[23] Lee YS, Zhang W. Modeling of heat transfer, fluid flow and solidification microstructure of nickel-base superalloy fabricated by laser powder bed fusion. Addit Manuf. 2016;12:178–188. doi:10.1016/j.addma.2016.05.003
[24] Yan W, Ge W, Qian Y, et al. Multi-physics modeling of single/multiple-track defect mechanisms in electron beam selective melting. Acta Mater. 2017;134:324–333. doi:10.1016/j.actamat.2017.05.061
[25] Tang C, Tan JL, Wong CH. A numerical investigation on the physical mechanisms of single track defects in selective laser melting. Int J Heat Mass Transf. 2018;126:957–968. doi:10.1016/j.ijheatmasstransfer.2018.06.073
[26] Zheng M, Wei L, Chen J, et al. A novel method for the molten pool and porosity formation modelling in selective laser melting. Int J Heat Mass Transf. 2019;140:1091–1105. doi:10.1016/j.ijheatmasstransfer.2019.06.038
[27] Tang C, Le KQ, Wong CH. Physics of humping formation in laser powder bed fusion. Int J Heat Mass Transf. 2020;149:119172. doi:10.1016/j.ijheatmasstransfer.2019.119172
[28] Yuan W, Chen H, Cheng T, et al. Effects of laser scanning speeds on different states of the molten pool during selective laser melting: Simulation and experiment. Mater Des. 2020;189:108542. doi:10.1016/j.matdes.2020.108542
[29] Ren Z, Zhang DZ, Fu G, et al. High-fidelity modelling of selective laser melting copper alloy: laser reflection behavior and thermal-fluid dynamics. Mater Des. 2021;207:109857. doi:10.1016/j.matdes.2021.109857
[30] Elahi SM, Tavakoli R, Boukellal AK, et al. Multiscale simulation of powder-bed fusion processing of metallic alloys. Comput Mater Sci. 2022;209:111383. doi:10.1016/j.commatsci.2022.111383
[31] Li E, Zhou Z, Wang L, et al. Modelling of keyhole dynamics and melt pool flow in laser powder bed fusion process. Powder Technol. 2022;400:117262. doi:10.1016/j.powtec.2022.117262
[32] Parivendhan G, Cardiff P, Flint T, et al. A numerical study of processing parameters and their effect on the melt-track profile in Laser Powder Bed Fusion processes. Addit Manuf. 2023;67:103482. doi:10.1016/j.addma.2023.103482
[33] Shrestha S, Chou K. A study of transient and steady-state regions from single-track deposition in laser powder bed fusion. J Manuf Process. 2021;61:226–235. doi:10.1016/j.jmapro.2020.11.023
[34] Chen H, Wei Q, Wen S, et al. Flow behavior of powder particles in layering process of selective laser melting: numerical modeling and experimental verification based on discrete element method. Int J Mach Tools Manuf. 2017;123:146–159. doi:10.1016/j.ijmachtools.2017.08.004
[35] Chen H, Sun Y, Yuan W, et al. A review on discrete element method simulation in laser powder bed fusion additive manufacturing. Chin J Mech Eng: Addit Manuf Front. 2022;1(1):100017. doi:10.1016/j.cjmeam.2022.100017
[36] Chen H, Wei Q, Zhang Y, et al. Powder-spreading mechanisms in powder-bed-based additive manufacturing: Experiments and computational modeling. Acta Mater. 2019;179:158–171. doi:10.1016/j.actamat.2019.08.030
[37] Aggarwal A, Shin YC, Kumar A. Investigation of the transient coupling between the dynamic laser beam absorptance and the melt pool - vapor depression morphology in laser powder bed fusion process. Int J Heat Mass Transf. 2023;201:123663. doi:10.1016/j.ijheatmasstransfer.2022.123663
[38] Wang L, Zhang Y, Yan W. Evaporation model for keyhole dynamics during additive manufacturing of metal. Phys Rev Appl. 2020;14(6):064039. doi:10.1103/PhysRevApplied.14.064039
[39] Jakumeit J, Zheng G, Laqua R, et al. Modelling the complex evaporated gas flow and its impact on particle spattering during laser powder bed fusion. Addit Manuf. 2021;47:102332. doi:10.1016/j.addma.2021.102332

[40] Young ZA, Guo Q, Parab ND, et al. Types of spatter and their features and formation mechanisms in laser powder bed fusion additive manufacturing process. Addit Manuf. 2020;36:101438. doi:10.1016/j.addma.2020.101438

[41] Chen H, Yan W. Spattering and denudation in laser powder bed fusion process: multiphase flow modelling. Acta Mater. 2020;196:154–167. doi:10.1016/j.actamat.2020.06.033

[42] Chen H, Zhang Y, Giam A, et al. Experimental and computational study on thermal and fluid behaviours of powder layer during selective laser melting additive manufacturing. Addit Manuf. 2022;52:102645. doi:10.1016/j.addma.2022.102645

[43] Le T-N, Lo Y-L, Chen K-Y, et al. Numerical and experimental investigation into powder entrainment and denudation phenomena in laser powder bed fusion process. Powder Technol. 2022;410:117907. doi:10.1016/j.powtec.2022.117907

[44] Li X, Zhao C, Sun T, et al. Revealing transient powder-gas interaction in laser powder bed fusion process through multi-physics modeling and high-speed synchrotron x-ray imaging. Addit Manuf. 2020;35:101362. doi:10.1016/j.addma.2020.101362

[45] Li X, Guo Q, Chen L, et al. Quantitative investigation of gas flow, powder-gas interaction, and powder behavior under different ambient pressure levels in laser powder bed fusion. Int J Mach Tools Manuf. 2021;170:103797. doi:10.1016/j.ijmachtools.2021.103797

[46] Yu T, Zhao J. Quantitative simulation of selective laser melting of metals enabled by new high-fidelity multiphase, multiphysics computational tool. Comput Methods Appl Mech Eng. 2022;399:115422. doi:10.1016/j.cma.2022.115422

[47] Uhlmann M. An immersed boundary method with direct forcing for the simulation of particulate flows. J Comput Phys. 2005;209(2):448–476. doi:10.1016/j.jcp.2005.03.017

[48] Knight CJ. Theoretical modeling of rapid surface vaporization with back pressure. AIAA J. 1979;17(5):519–523. doi:10.2514/3.61164

[49] Hertz H. Ueber die Verdunstung der Fl¨ussigkeiten, insbesondere des Quecksilbers, im luftleeren Raume. Ann Phys Chem. 1882;17:177–193. doi:10.1002/andp.18822531002

[50] Klassen A, Scharowsky T, Körner C. Evaporation model for beam based additive manufacturing using free surface lattice Boltzmann methods. J Phys D: Appl Phys. 2014;47(27):275303. doi:10.1088/0022-3727/47/27/275303

[51] Cook PS, Murphy AB. Simulation of melt pool behaviour during additive manufacturing: underlying physics and progress. Addit Manuf. 2020;31:100909. doi:10.1016/j.addma.2019.100909

[52] Hirt CW, Nichols BD. Volume of fluid (VOF) method for the dynamics of free boundaries. J Comput Phys. 1981;39(1):201–225. doi:10.1016/0021-9991(81)90145-5.

[53] Cho J-H, Na S-J. Implementation of real-time multiple reflection and Fresnel absorption of laser beam in keyhole. J Phys D: Appl Phys. 2006;39(24):5372–5378. doi:10.1088/0022-3727/39/24/039

[54] Ducharme R, Williams K, Kapadia P, et al. The laser-welding of thin metal sheets - an integrated keyhole and weld pool model with supporting experiments. J Phys D Appl Phys. 1994;27(8):1619–1627. doi:10.1088/0022-3727/27/8/006

[55] Bayat M, Thanki A, Mohanty S, et al. Keyhole-induced porosities in laser-based powder bed fusion (L-PBF) of Ti6Al4V: high-fidelity modelling and experimental validation. Addit Manuf. 2019;30:100835. doi:10.1016/j.addma.2019.100835

[56] Carman PC. Fluid flow through granular beds. Trans Inst Chem Eng Lond. 1937;15:150–156.

[57] Chang S, Stefanescu D. A model for macrosegregation and its application to Al-Cu castings. Metall Mater Trans A. 1996;27:2708–2721. doi:10.1007/BF02652365

[58] Di Renzo A, Di Maio FP. Comparison of contact-force models for the simulation of collisions in DEM-based granular flow codes. Chem Eng Sci. 2004;59(3):525–541. doi:10.1016/j.ces.2003.09.037

[59] Chaudhuri B, Muzzio FJ, Tomassone MS. Modeling of heat transfer in granular flow in rotating vessels. Chem Eng Sci. 2006;61(19):6348–6360. doi:10.1016/j.ces.2006.05.034

[60] Cheng GJ, Yu AB, Zulli P. Evaluation of effective thermal conductivity from the structure of a packed bed. Chem Eng Sci. 1999;54(19):4199–4209. doi:10.1016/S0009-2509(99)00125-6

[61] Norouzi HR, Zarghami R, Sotudeh-Gharebagh R, et al. *Coupled CFD-DEM modeling: formulation, implementation and application to multiphase flows*. New York: John Wiley & Sons; 2016. doi:10.1002/9781119005315.fmatter

[62] Ranz WE. Evaporation from drops-I and-II. Chem Eng Progr. 1952;48(141-146):173–180.

[63] Murphy AB, Arundell CJ. Transport coefficients of argon, nitrogen, oxygen, argon-nitrogen, and argon-oxygen plasmas. Plasma Chem Plasma Process. 1994;14(4):451–490. doi:10.1007/BF01570207

[64] Chia HY, Wang L, Yan W. Influence of oxygen content on melt pool dynamics in metal additive manufacturing: high-fidelity modeling with experimental validation. Acta Mater. 2023;249:118824. doi:10.1016/j.actamat.2023.118824

[65] Wang L, Zhang Y, Chia HY, et al. Mechanism of keyhole pore formation in metal additive manufacturing. npj Comput Mater. 2022;8(1):22. doi:10.1038/s41524-022-00699-6

[66] S.D.I. Software, Simcenter STAR-CCM user guide v.2020.3. (2020.

[67] Masoomi M, Soltani-Tehrani A, Shamsaei N, et al. Convection heat transfer coefficients for laser powder bed fusion. 2018.

[68] Chen D, Li G, Wang P, et al. Numerical simulation of melt pool size and flow evolution for laser powder bed fusion of powder grade Ti6Al4 V. Finite Elem Anal Des. 2023;223:103971. doi:10.1016/j.finel.2023.103971

[69] Guo L, Wang H, Liu H, et al. Understanding keyhole induced-porosities in laser powder bed fusion of aluminum and elimination strategy. Int J Mach Tools Manuf. 2023;184:103977. doi:10.1016/j.ijmachtools.2022.103977

[70] Knapp GL, Coleman J, Rolchigo M, et al. Calibrating uncertain parameters in melt pool simulations of additive manufacturing. Comput Mater Sci. 2023;218:111904. doi:10.1016/j.commatsci.2022.111904

[71] Ansari P, Salamci MU. On the selective laser melting based additive manufacturing of AlSi10Mg: the process parameter investigation through multiphysics simulation

and experimental validation. J Alloys Compd. 2022;890:161873. doi:10.1016/j.jallcom.2021.161873
[72] Katagiri J, Kusano M, Nomoto S, et al. Influence of recoil pressure, mushy zone flow resistance and reflectivity on melt pool shape in laser powder bed fusion simulation. Case Stud Therm Eng. 2023;50:103477. doi:10.1016/j.csite.2023.103477
[73] Yao LM, Huang S, Ramamurty U, et al. On the formation of "Fish-scale" morphology with curved grain interfacial microstructures during selective laser melting of dissimilar alloys. Acta Mater. 2021;220:117331. doi:10.1016/j.actamat.2021.117331
[74] Zheng H, Wang Y, Xie Y, et al. Observation of vapor plume behavior and process stability at single-track and multi-track levels in laser powder bed fusion regime. Metals. 2021;11(6):937. doi:10.3390/met11060937
[75] Fabbro R, Slimani S, Doudet I, et al. Experimental study of the dynamical coupling between the induced vapour plume and the melt pool for Nd–Yag CW laser welding. J Phys D: Appl Phys. 2006;39(2):394–400. doi:10.1088/0022-3727/39/2/023
[76] Pang S, Chen X, Shao X, et al. Dynamics of vapor plume in transient keyhole during laser welding of stainless steel: local evaporation, plume swing and gas entrapment into porosity. Opt Lasers Eng. 2016;82:28–40. doi:10.1016/j.optlaseng.2016.01.019
[77] Li Z, Yu G, He X, et al. Vapor-induced flow and its impact on powder entrainment in laser powder bed fusion. Mater Today Commun. 2023;36:106669. doi:10.1016/j.mtcomm.2023.106669
[78] Li Z, Li H, Yin J, et al. A review of spatter in laser powder bed fusion additive manufacturing: in situ detection, generation, effects, and countermeasures. Micromachines. 2022;13(8):1366. doi:10.3390/mi13081366
[79] Liu J, Wen P. Metal vaporization and its influence during laser powder bed fusion process. Mater Des. 2022;215:110505. doi:10.1016/j.matdes.2022.110505
[80] Yuan W, Chen H, Peng C, et al. Revealing melt-vapor-powder interaction towards laser powder bed fusion process via DEM-CFD coupled model. Surf Sci Technol. 2023;1(1):14. doi:10.1007/s44251-023-00014-5
[81] Qu M, Guo Q, Escano LI, et al. Mitigating keyhole pore formation by nanoparticles during laser powder bed fusion additive manufacturing. Addit Manuf Lett. 2022;3:100068. doi:10.1016/j.addlet.2022.100068
[82] Zhao C, Guo Q, Li X, et al. Bulk-explosion-induced metal spattering during laser processing. Phys Rev X. 2019;9(2):021052. doi:10.1103/PhysRevX.9.021052
[83] Khairallah SA, Sun T, Simonds BJ. Onset of periodic oscillations as a precursor of a transition to pore-generating turbulence in laser melting. Addit Manuf Lett. 2021;1:100002. doi:10.1016/j.addlet.2021.100002
[84] Nassar AR, Gundermann MA, Reutzel EW, et al. Formation processes for large ejecta and interactions with melt pool formation in powder bed fusion additive manufacturing. Sci Rep. 2019;9(1):5038. doi:10.1038/s41598-019-41415-7
[85] Ly S, Rubenchik AM, Khairallah SA, et al. Metal vapor micro-jet controls material redistribution in laser powder bed fusion additive manufacturing. Sci Rep. 2017;7(1):4085. doi:10.1038/s41598-017-04237-z
[86] Ikeshoji TT, Yonehara M, Kato C, et al. Spattering mechanism of laser powder bed fusion additive manufacturing on heterogeneous surfaces. Sci Rep. 2022;12(1):20384. doi:10.1038/s41598-022-24828-9
[87] Khairallah SA, Martin AA, Lee JRI, et al. Controlling interdependent meso-nanosecond dynamics and defect generation in metal 3D printing. Science. 2020;368(6491):660–665. doi:10.1126/science.aay7830
[88] Huang Y, Shen C, Ji X, et al. Correlation between gas-dynamic behaviour of a vapour plume and oscillation of keyhole size during laser welding of 5083 Al-alloy. J Mater Process Technol. 2020;283:116721. doi:10.1016/j.jmatprotec.2020.116721
[89] Caprio L, Demir AG, Previtali B. Observing molten pool surface oscillations during keyhole processing in laser powder bed fusion as a novel method to estimate the penetration depth. Addit Manuf. 2020;36:101470. doi:10.1016/j.addma.2020.101470
[90] Bitharas I, Burton A, Ross AJ, et al. Visualisation and numerical analysis of laser powder bed fusion under cross-flow. Addit Manuf. 2021;37:101690. doi:10.1016/j.addma.2020.101690
[91] Zhirnov I, Kouprianoff D. Acoustic diagnostic of laser powder bed fusion processes. In: 10th Swedish Production Symposium, SPS 2022; vol. 21. IOS Press; 2022. p. 542–552. doi:10.3233/ATDE220173
[92] Chen Z, Wang D, Zhang Y. Microphone signal specialities in laser powder bed fusion: single-track scan and multi-track scan. J Mater Res Technol. 2023;24:1344–1362. doi:10.1016/j.jmrt.2023.03.091
[93] Ebrahimi A, Kleijn CR, Richardson IM. A simulation-based approach to characterise melt-pool oscillations during gas tungsten arc welding. Int J Heat Mass Transf. 2021;164:120535. doi:10.1016/j.ijheatmasstransfer.2020.120535
[94] Xu J-Y, Yuan W-H, Zhang C, et al. Improving the processability and grain structures of additively manufactured Al-Fe-Cu-xZr alloy: experiment and high-fidelity simulation. Addit Manuf. 2024;84:104074. doi:10.1016/j.addma.2024.104074
[95] Nath P, Sato M, Karve P, et al. Multi-fidelity modeling for uncertainty quantification in laser powder bed fusion additive manufacturing. Integr Mater Manuf Innov. 2022;11(2):256–275. doi:10.1007/s40192-022-00260-9
[96] Menon N, Mondal S, Basak A. Multi-fidelity surrogate-based process mapping with uncertainty quantification in laser directed energy deposition. Materials. 2022;15(8):2902. doi:10.3390/ma15082902